Loss of the mitochondrial carrier, *SLC25A1,* during embryogenesis induces a unique senescence program controlled by p53

Anna Kasprzyk-Pawelec[1], Mingjun Tan[1,2], Raneen Rahhal[1], Alec McIntosh[1], Harvey Fernandez[1,3], Rami Mosaoa[1,4], Lei Jiang[5], Gray W. Pearson[1], Eric Glasgow[1], Jerry Vockley[6], Christopher Albanese[1], and Maria Laura Avantaggiati[1,#]

7

8 [1] Georgetown University Medical Center, Lombardi Comprehensive Cancer Center, Washington,
9 D.C., USA
10 [2] Penn State College of Medicine, Department of Cellular & Molecular Physiology, Hershey, PA, USA
11 [3] University of Virginia Medical Center, Charlottesville, VA, USA.
12 [4] Department of Biochemistry, Faculty of Science, King Abdulaziz University, Jeddah, Saudi Arabia
13 [5] Department of Molecular and Cellular Endocrinology, Arthur Riggs Diabetes and Metabolism
14 Research Institute, City of Hope Medical Center, Comprehensive Cancer Center, City of Hope
15 Medical Center, Duarte, CA, USA
16 [6] Department of Pediatrics, Division of Genetic and Genomic Medicine, UPMC Children's Hospital of
17 Pittsburgh, Pittsburgh, PA, USA

18

19 **#** Correspondence:
20 Maria Laura Avantaggiati: ma364@georgetown.edu

ABSTRACT

Germline inactivating mutations of the SLC25A1 gene contribute to various human developmental disorders, including combined D/L-2-hydroxyglutaric aciduria (D/L-2HGA), a severe systemic syndrome characterized by the accumulation of both enantiomers of 2-hydroxyglutaric acid (2HG). The mechanisms by which SLC25A1 deficiency leads to this disease and the role of 2HG are unclear and no therapies exist. We now show that mice lacking both Slc25a1 alleles display a spectrum of alterations that resemble human D/L-2HGA. Mechanistically, SLC25A1 loss results in a proliferation defect and activates two distinct senescence pathways, oncogene-induced senescence (OIS) and mitochondrial dysfunction-induced senescence (MiDAS), both involving the p53 tumor suppressor and driven by two discernible signals: the accumulation of 2HG, inducing OIS, and mitochondrial dysfunction, triggering MiDAS. Inhibiting these senescence programs or blocking p53 activity reverses the growth defect caused by SLC25A1 dysfunction and restores proliferation. These findings reveal novel pathogenic roles of senescence in human disorders and suggest potential strategies to correct the molecular alterations caused by SLC25A1 loss.

57 **INTRODUCTION**

58 The solute carrier family member SLC25A1, also known as CTP/CIC, belongs to a family of nuclear
59 encoded ion transporters localized in the inner mitochondrial membrane where it promotes the bi-
60 directional exchange of citrate between the mitochondria and the cytosol (Mosaoa et al, 2021;
61 Palmieri et al, 2020; Ruprecht and Kunji, 2020). In the cytoplasm, citrate is a substrate for *de novo*
62 lipid synthesis (DNL), while in the mitochondria it feeds into the tricarboxylic acid (TCA) cycle. The
63 human *SLC25A1* gene maps to chromosome *22q11.2*. Heterozygous microdeletions of this region
64 give raise to Velocardiofacial (VCFS) and DiGeorge (DGS) syndromes (Funato, 2022; Maynard et al,
65 2008), a group of developmental disorders associated with loss of 30 to 40 genes in addition to
66 *SLC25A1*. Patients with *22q11.2* deletion syndrome present with heart malformations, cleft palate,
67 immune deficiency due to thymic aplasia, short stature and abnormal facial features, particularly
68 microcephaly, malposition of the ears, small eyes, underdeveloped chin and flat midface. We and
69 others have previously shown that the knock-down of the *slc25a1a* homologous gene in zebrafish
70 embryos induces craniofacial and heart abnormalities, suggesting a role for SLC25A1 in the
71 pathogenesis of *22q11.2* deletion syndromes (Catalina-Rodriguez et al, 2012; Chaouch et al, 2014).
72

73 Various *SLC25A1* gene mutations have also been reported in a group of developmental disorders
74 characterized by D/L-hydroxyglutaric aciduria (D/L-2HGA), a disease hallmarked by the accumulation
75 and urinary escretion of the D- and L- enantiomeric forms of 2-hydroxyglutarate (2HG) (Pop et al,
76 2018; Edvardson et al, 2016; Prasun et al, 2015; Nota et al, 2015; Smith et al, 2013; Kranendijk et al,
77 2012). The clinical spectrum of manifestations associated with *SLC25A1* gene mutations in D/L-
78 2HGA is very severe, consisting of a variety of craniofacial abnormalities, including facial dysmorphic
79 features, down-slanting of the eyes, ear abnormalities, micrognathia or retrognathia, flat nose and
80 microcephaly or macrocephaly (Pop et al, 2018). In addition, these patients present with
81 developmental delay, brain abnormalities, (cerebral atrophy, agenesis of the corpus callosum), and
82 with respiratory insufficiency, epilepsy, encephalopathy and occasionally, cardiomyopathy (Kranendijk
83 et al, 2012). Unlike in VCFS/DGS, where only one allele of the *SLC25A1* gene is lost, D/L-2HG-
84 aciduria results from homozygous or compound heterozygous mutations that typically involve a

85 profound disruption of the citrate transport activity. We and others have previously reported that the
86 most severe cases of D/L-2HGA are sustained by the compound heterozygous alleles,
87 p.Ala9Profs*82 and p.Pro45Leu (onset at 1 day, death at 1 month) (Prasun et al, 2015;, Pop et al,
88 2018), which results in complete loss of SLC25A1 mitochondrial activities. In all other cases, with few
89 exceptions, there is a strong correlation between the extent of loss of export activity and the severity
90 of the clinical manifestations.
91
92 It is currently unknown whether 2HG plays a direct role in the pathogenesis of SLC25A1-associated
93 D/L-2HGA. Both enantiomers are derived from the reduction of 2-oxoglutarate (α-ketoglutarate, αKG)
94 and there are different pathways for 2HG production and elimination (Fig. 1A) (Du et al., 2022; Ježek
95 2020; Losman and Kaelin, 2013). Individual forms of L- or D-2HGA are caused by mutations in the 2-
96 hydroxyglutarate dehydrogenases L- (*L2HGDH*), or D- (*D2HGDH*) which eliminate each enantiomer
97 by oxidation to αKG. Gain of function, mutant forms of *isocitrate dehydrogenase 1 or 2* (*IDH1*/2)
98 convert αKG to D-2HG, and *IDH2* mutations can also cause D-2HGA (Losman and Kaelin, 2013;
99 Kranendijk et al, 2012). Mechanistically, D/L-2HG have been extensively characterized in the context
100 of tumors harboring genetic mutations of *IDH1/2* (Ježek, 2020). However, these gain of function
101 proteins produce extraordinarily high (10-30mM) amounts of 2HG. By contrast, it was initially noted
102 that while combined D/L-2HGA is clinically more severe, the levels of D-2HG and L-2HG in these
103 patients are very moderately elevated compared to other forms of 2HGA and this was considered a
104 distinct feature of D/L-2HGA (Kranendijk et al, 2012). Furthermore, distinct biochemical alterations
105 clearly separate D/L-2HGA sustained by SLC25A1 deficiency from other forms of 2HGA, particularly
106 the presence of increased lactate and TCA cycle intermediates in the urine, indicative of
107 mitochondrial dysfunction (Smith et al, 2016; Cohen et al, 2018; Prasun et al, 2015). Indeed, we have
108 documented that genetic or pharmacologic inhibition of SLC25A1 in tumor cells impairs mitochondrial
109 oxidative phosphorylation (OXPHOS) and rewires the metabolism towards glycolysis, essentially
110 driving a Warburg effect (Mosaoa et al, 2021; Fernandez et al, 2018). However, whether and how
111 SLC25A1 dysfunction influences mitochondrial activity in human diseases is currently uknown.
112

113 In keeping with the activity of SLC25A1 in the transport of citrate, the current model envisions that a
114 deficit in the cytosolic citrate pool hampers *de novo* lipid synthesis (DNL). Indeed, the only therapy
115 that has been so far attempted in D/L-2HGA patients consists of oral administration of citrate, but the
116 prognosis of D/L-2HGA is poor and the effects of citrate complementation remain controversial (Phua
117 et al, 2024). In the present work we now show that mice lacking both *Slc25a1* alleles exhibit several
118 phenotypic characteristics typical of VCFS and DGS as well as of D/L-2HGA. Mechanistically, loss of
119 SLC25A1 activity leads to a severe deficit of proliferative capacity and uniquely triggers two distinct
120 pathways of cellular senescence, mitochondrial dysfunction associated senescence (MiDAS) and
121 oncogene induced senescence (OIS). We identify several potential corrective strategies to reverse
122 these senescence programs, potentially opening novel strategies for therapeutic intervention in these
123 diseases.
124
125
126
127
128
129
130
131
132
133
134
135
136
137
138
139
140

141 **RESULTS**

142

143 **Loss of the *Slc25a1* gene during embryogenesis disrupts multiple organs development.** To
144 understand the role of SLC25A1, we began by studying the pattern of expression of SLC25A1 protein
145 in normal murine embryonic tissues. The analysis of different organs of *Slc25a1* wild-type embryos at
146 19.5 days post-fertilization (dpf) by immunoblot showed strong expression in the brain, heart, lung,
147 liver, colon spleen and pancreas (Fig. 1B). This finding was confirmed with immunohistochemistry
148 (Fig. 1C,D). Immunofluorescence of the head showed specific enrichment of SLC25A1 protein in the
149 mitochondria, as revealed by staining with mitofilin (Fig. 1E,F). Within the craniofacial region,
150 SLC25A1 signal was particularly strong in the frontal region, in the mouth, eyes, palate and tongue,
151 as well as in the brain and cerebellum, all sites affected in human diseases sustained by its deficiency
152 (Fig. 1C-E).

153

154 To understand the impact of SLC25A1 activity, we generated a knock-out mouse model. Mice
155 harboring a heterozygous germline targeted deletion in one *Slc25a1* allele were produced by the
156 Mutant Mouse Resource & Research Centers (MMRRC, C57BL/6-tm1a) with a targeting vector which
157 is based upon the 'knockout-first' allele, as we have described previously (Tan et al, 2020). In this
158 vector, an *IRES:lacZ* trapping cassette and a *floxed* promoter-driven neo cassette is inserted between
159 intron *1* and *2* of the *Slc25a1* gene on chromosome 16 (EV1A,B). We first expanded a population of
160 heterozygous *Slc25a1*$^{+/-}$ mice, and intercrosses of these animals subsequently allowed studying the
161 population of homozygous mutants. These null mice completely lacked SLC25A1 protein and mRNA
162 in all tissues examined (Fig. 2A and EV1C,D). Relative to wild-type and heterozygous animals,
163 *Slc25a1*$^{-/-}$ null mice were detected at roughly normal Mendelian ratio (Fig. 2B). However, only few of
164 them were born, succumbing immediately after birth (Fig. 2C). Importantly, these embryos were be
165 detected at all stages of development from day 7 to day 19-21 dpf (EV1), indicating that the knock-out
166 of the *Slc25a1* gene leads to a highly penetrant perinatal lethal phenotype, but is not overtly
167 embryonic lethal. By contrast, *Slc25a1* heterozygous showed no obvious defects and normal lifespan,
168 which we followed up to 1 year. The analysis of the *Slc25a1*$^{-/-}$ embryos at different stages of

169 development revealed a substantial spectrum of alterations affecting multiple organs. The majority of
170 them displayed small body size and anemia/pallor (Fig. 2D-G), malformation/absence of the ears,
171 absence of one or both eyes, as well as cleft palate (Fig. 2E-G). The cranio-facial region and the
172 brain were the most affected and 43% of embryos showed overt defects in neural tube closure,
173 manifested by exencephaly or anencephaly. A repository of computed tomography (CT) images
174 available through the mouse phenotype consortium at UC Davis (Groza et al, 2023; Dickinson et al,
175 2016), confirmed that the craniofacial region of *Slc25a1*$^{-/-}$ embryos was severely dysmorphic often
176 with unrecognizable anatomic features, including bulging or absent eyes, dilated turbinates, enlarged
177 and protruding tongue (Fig. 2H,I and EV2A). Brain and liver hemorrhage (EV2B), heart alterations,
178 gastroschisis (Fig. 2H^{3} and EV2B), and bone abnormalities were also present. These latter were
179 significant and include lack of skull (Fig. 2E and 2G), pectus excavatum (Fig. 2H^{4}), abnormal
180 curvatures and thickness of the spine and increased cartilage content in the vertebral column
181 reminiscent of enchondromatosis (Fig. 2H^{3} and EV2CD). Interestingly, although we have not
182 quantified these latter abnormalities, pectus excavatum, enchondromatosis and hemorrhages were
183 previously described in mice harboring knock-in mutations of gain of function mutant *IDH1/2* alleles
184 (Hirata et al, 2015; Sasaki et al, 2012). H&E staining and scanning electron microscopy (SEM)
185 performed on the brain and craniofacial region revealed prominent disorganization in the developing
186 neocortex of *Slc25a1*$^{-/-}$ embryos at E18 dpf, which showed diffused areas of nuclear pleomorphism
187 with alterations in nuclear size, disorganization of the stroma, and mis-orientation of neurons in the
188 distinctive cortical layers (Fig. 2I,J). Alterations in the mitochondrial morphology were also clearly
189 detected (not shown). The comparison of chondroblasts and collagen from the nose cartilage
190 revealed morphological differences, with an increase in cytoplasmic vacuolization seen in *Slc25a1*
191 deficient animals, and disruption in the directionality of collagen fibers in the matrix (Fig. 2K). In
192 addition, the tongue of virtually all *Slc25a1*$^{-/-}$ mice appeared abnormal in size and protruding, with
193 thicker myocytes, altered directionality of fiber packages and increased connective tissue (Fig. 2I,L).
194 Thus, systemic loss of the *SLC25A1* gene during embryonic development recapitulates but also
195 severely expands the spectrum of alterations seen in human DGS/VCFS and in D/L-2HGA.
196

197 **SLC25A1 deficient embryos undergo metabolic and transcriptional rewiring.** The current model
198 envisions that the pathogenesis of diseases due to impaired SLC25A1 activity is sustained by the
199 deficit of citrate export from the mitochondria to the cytosol, which results in impairment of lipids
200 synthesis. We tested this model by performing targeted and untargeted metabolomic and lipidomic
201 analyses, paralleled by immuno-blot experiments interrogating the main pathways involved in lipid
202 biosynthesis. The levels of the key rate-limiting, lipogenic enzymes, fatty acid synthase (FASN) and
203 acetyl-CoA carboxylase Alpha (ACC1) were up-regulated in the brains and MEFs derived from
204 *Slc25a1*$^{-/-}$ mice, at both the protein and mRNA levels (Fig. 3A-C). Given the herogeneity of the
205 phenotypes of Slc25a1 deficient embryos and of the clinical manifestations of D/L2HGDH, for the
206 metabolomic analyses we employed five wild-type and five *Slc25a1* null mice exhibiting different
207 phenotypes, spanning from nearly normal to severe (EV2E). In spite of such heterogeneity, the
208 principal component analysis (PCA) and the Partial Least Squares (PLS) revealed a good separation
209 between these samples with the homozygous null mice clustering together (Fig.3D). Global
210 metabolomic analysis showed that the main alteration consisted of enhanced triglyceride species in
211 the brains and amniotic fluids (Fig. 3E,F), and enrichment in linoleic acid, phospholipids, glycerolipids,
212 sphingolipids, arachidonic-, steroid-, and bile acid biosynthetic pathway, along with an increase in the
213 Warburg effect (Fig. 3G). Importantly, the concentration of αKG, the precursor of 2HG, and of citrate
214 were elevated *Slc25a1*$^{-/-}$ mice, and itaconate, which is derived from cytosolic citrate *via* the activity of
215 Immune-Responsive Gene 1, *IRG1*, was increased (Fig. 3H), suggesting an excess of cytosolic
216 citrate.
217
218 To then identify the pathways altered in an SLC25A1-dependent manner and particularly differences
219 relative to the severity of alterations, we conducted a phenotype-to-transcriptome comparison using
220 *Slc25a1*$^{-/-}$ mice with varying phenotypic alterations, classified as severe (E-SEV) or moderate (E-
221 MOD) (Fig. 4A). E-SEV mice displayed critical abnormalities, including severe facial deformities like
222 anophthalmia and cleft palate, transparent skin, along with brain alterations common in *Slc25a1*
223 deficient embryos. Global transcriptome and hierarchical clustering identified 1395 genes uniquely
224 regulated in *Slc25a1* homozygous mutants with most differentially regulated genes being up-

225 regulated (Fig. 4B,C). These included: genes involved in inflammatory and pro-oncogenic pathways
226 (Immune Cytokine Signaling, Signaling by NRTKs, AP1 Transcription & MAPK Signaling), the hypoxia
227 response and, surprisingly, senescence (Fig. 4D), along with an enrichment of tumor-associated
228 transcriptional signatures involved in breast cancer, neuroblastoma, ovarian cancer, and others, as
229 well as induction of the p53 tumor suppressor (Fig. 4E). Using the transcriptomic data derived from
230 each of the embryos (Fig. 4F), we then employed a Hue-Saturation-Value (HSV) analysis and the
231 Enrichr gene set tool, to identify genes that are significantly more active in E-SEV and moderately
232 elevated in E-MOD *versus* wild-type (*WT* **>** *E-MD* **>>** *E-SV);* $p < 0.05$) (Xie et al, 2021; Kuleshov et al,
233 2016). This approach revealed that the top up-regulated signals in the E-SEV are the hypoxia
234 response, along with pro-inflammatory (TNFα, IL-6) and pro-oncogenic pathways, including mTORC,
235 the KRas pathways, and the induction of the Epithelial to Mesenchymal Transition (EMT) (Fig. 4G). In
236 addition, both glycolysis and cholesterol responses were enhanced, consistent with the previous
237 metabolic analysis.
238
239 We conclude that in this mouse model, SLC25A1 is not rate limiting for maintenance of the citrate and
240 lipid pool during embryonic development as generally thought, and consistent with the well
241 documented existence of multiple pathways able to replenish cytosolic citrate in cells lacking
242 SLC25A1, including *via* glutamine reductive carboxylation (Mosaoa et al, 2021; Jiang et al, 2017;
243 Jiang et al, 2016;). Instead, SLC25A1 loss rewires the transcriptome towards senescence, pro-
244 oncogenic and inflammatory signals and induces an hypoxic response.
245
246 **SLC25A1 loss induces the IOS and MiDAS pathways of senescence.** We next examined the
247 growth properties of embryo fibroblasts (MEFs) derived from mice, as well as of clinically relevant
248 samples, using skin fibroblasts from two newborn patients affected by D/L-2HG-aciduria, patient 893
249 (male) and patient 897 (female) (Phua et al, 2024). Both the *Slc25a1*$^{-/-}$ MEFs cells and the patient-
250 derived fibroblasts exhibited a proliferation defect at early passages (Fig. 5A and not shown). This
251 loss of proliferative capacity was highly suggestive of premature senescence, which when aberrantly
252 induced during embryonic development drives neuro-developmental and neural tube closure defects

253 (Klein et al, 2023; Rhinn et al, 2022; Xu et al, 2021). Consistent with the transcriptomic analysis and
254 with the idea that loss of Slc25a1 induces senescence, the *Slc25a1*$^{-/-}$ MEFs as well the patients
255 fibroblasts showed a strong senescence-associated beta-galactosidase (SAβ-GAL) signal, the typical
256 hallmark of senescent cells (Fig. 5B-E). Further, the head and brain of *Slc25a1*$^{-/-}$ mice harvested at
257 late development stage (E19 dpf), reacted with antibodies directed against p21, a key mediator of
258 senescence (Fig. 5F,G). To rule out that senescence is the result of passaging primary cells in
259 culture and and to establish the relevance of the Slc25a1 transport activity, we conducted acute
260 SLC25A1 knock-down experiments, or we employed the specific SLC25A1 ihibitor (SLC25A1-i)
261 (Mosaoa et al, 2021). The shRNA, as well as the SLC25A1-i induced SAβ-GAL activity and arrest at
262 the G1/G2 phase of the cell cycle (Fig. 5H,I), demonstrating a direct effect of SLC25A1 inhibition in
263 the induction of the senescence arrest.
264
265 Senescent cells secrete many factors known as the Senescence-Associated Secretory Phenotype
266 (SASP), which differ depending upon the upstream triggering signal(s) (Fig. 6A). Oncogene induced
267 senescence (OIS), is characterized by secretion of pro-inflammatory mediators IL-6, IL-1β, and IL-1α,
268 and involves NFkB, mTOR, AP1/MAPK signaling, and the JAK/STAT pathway (Schmitt et al., 2022;
269 Wang et al., 2022; Cuollo et al., 2020; Xu et al., 2015). Due to DNA replication stress imposed by
270 oncogenes, OIS is associated with the DNA damage response, hallmarked by induction of
271 phosphorylated histone gamma H2AX and of the kinase Chk1/2 (Poehlmann A et al, 2011). A
272 second form of senescence, mitochondrial dysfunction-induced senescence (MiDAS) contributes to
273 accelerated aging in murine models of progeroid syndromes (Wile et al., 2016), and instead lacks pro-
274 inflammatory cytokines while recruiting the activity of AMPk, TNFα, and of anti-inflammatory IL-10,
275 among others (Wiley and Campisi, 2021; Wiley et al., 2016; Gomes et al., 2013). MiDAS occurs when
276 the NAD+/NADH ratio drops, leading to mitochondrial dysfunction and activation of the hypoxia
277 inducible factor, HIF1α in normoxic conditions, defined as a pseudo-hypoxia response. Both OIS and
278 MiDAS activate p53 to enforce growth arrest.
279

280 The analysis of the senescence program driven by SLC25A1 loss revealed a robust increase in IL-1β,
281 IL-6, γH2AX, Chk1 and mTOR indicative of OIS, along with IL-10, TNFα and AMPk which are typical
282 of MiDAS (Fig. 6B-D). Further, the levels of HIF1α were increased in the *Slc25a1*$^{-/-}$ MEFs cultured *in*
283 *vitro* in normoxic conditions, suggestive of a pseudo-hypoxia response (Fig. 6C), and p53 and p21
284 were induced in both the *Slc25a1* deficient mice and in the patient-derived fibroblasts indicative of
285 senescence arrest (Fig. 6C-E). Consistent with the previous transcriptomic data, the levels of
286 mTORC, which plays a role in nutrient sensing and also as a mediator of senescence associated to
287 aging (Weichhart, 2018), were elevated in most of these brains (Fig. 6F).
288
289 Collectively, these findings support the notion that loss of SLC25A1 leads to the simultaneous
290 activation of both the IOS and MiDAS pathway. Given these results, we next investigated the
291 molecular mechanisms by which SLC25A1 deficiency drives the MiDAS and IOS response.
292
293 **SLC25A1 dysfunction impairs OXPHOS *via* depletion of NAD$^+$ and enhanced PDK1-mediated**
294 **glycolysis.** The NAD$^+$/NADH ratio is a key determinant of OXPHOS. Several steps in the TCA cycle
295 generate NADH from NAD+ and this chain of reactions is necessary for respiration *via* the activity of
296 Complex-I (CI), which donates the electrons derived from NADH to other respiratory complex
297 subunits within the electron transport chain (ETC). First, we determined that the *Slc25a1*$^{-/-}$ MEFs
298 exhibited a severe deficit in the basal (BR), maximal (MR) and spare respiratory capacity (SRC) and
299 of ATP production (Fig. 7A), coinciding with a significant loss of function of complex I, II and III and V
300 (Fig. 7B). A similar respiratory deficit was recently described in the patient fibroblasts (Puah et al,
301 2024). In addition, cells lacking SLC25A1 prominently turned on glycolysis (Fig. 7C), which consumes
302 NAD$^+$ because many glycolytic enzymes use NAD$^+$ as a co-factor (Xie et al, 2020). To then establish
303 whether SLC25A1 dysfunction depletes NAD$^+$ at least in part by turning on glycolysis, we again
304 turned to a controlled cellular system where SLC25A1 activity was inhibited with the SLC25A1-i. By
305 using an enzymatic activity assay that assesses the ability of lactate dehydrogenase-A, LDH-A, to
306 carry out the oxidation of endogenous lactate to pyruvate, which reduces NAD$^+$ to NADH, we found a

307 stark 20 fold increase in the rates of conversion of NAD^+ to NADH in cells treated with SLC25A1-i
308 (Fig. 7D). Accordingly, the NAD^+/NADH ratio was strongly reduced in the *Slc25a1*$^{-/-}$ MEFs (Fig. 7E).
309
310 To identify the mechanisms leading to defective mitochondrial OXPHOS we focused on the pseudo-
311 hypoxia response and on the glycolytic switch. Consistent with prior data, the brains of *Slc25a1*$^{-/-}$
312 mice were significantly enriched in glycolytic- and HIF1- signal pathways (Fig.4 and not shown), as
313 well as in glycolytic genes that are under direct transcriptional control of HIF1α. These include the
314 kinases PDK1 and PDK2, glucose transporters (MCT4, GLUT4), LDH-A, Enolase (ENO1), and
315 glucose-phosphate-isomerase 1 (GPI1) (Fig. 7F). PDK1 inhibits the pyruvate dehydrogenase
316 complex, PDH, preventing the conversion and entry of acetyl-CoA into the TCA cycle for OXPHOS,
317 while enhancing its reduction to lactate. To then directly test the relevance of this pathway, we
318 explored the activity of the PDK1 and glycolytic inhibitor dichloroacetate (DCA). As shown in Figure
319 7G, a short time treatment (4 hours) of the *Slc25a1*$^{-/-}$ MEFs with DCA significantly rescued the rates
320 of OCR as well as of ATP production, to levels nearly comparable to wild-type MEFs. Similar results
321 were obtained by supplementing cells with the cell permeable, NAD^+ precursor Nicotinamide
322 mononucleotide**,** NMN, which also partially rescued the rates of OXPHOS (Fig. 7H).
323
324 Albeit we cannot exclude that additional mechanisms are involved in the reduced OXPHOS rates
325 driven by SLC25A1 deficiency, these data importantly demonstrate that the glycolytic switch is not
326 simply a compensatory response to impaired mitochondrial respiratory activity, but is actually a driver
327 of mitochondrial dysfunction and imply that such respiratory deficit can at least partially be corrected.
328
329 **In cells lacking SLC25A1 low levels of 2HG are produced by wild-type IDH1 and induce IOS***.* It
330 was noted before that in combined D/L-2HG-aciduria caused by SLC25A1 impairment the
331 concentrations of D-2HG and L-2HG are moderately increased compared to individual forms of L- or
332 D-2HG-aciduria, which result from mutations of the *IDH1/2* or *D/L-2HGDH* genes and leads to high
333 millimolar levels of these enantiomers (Ježek et al, 2020; Kranendijk et al, 2012). In agreement with
334 these previous observations, we determined that the total pool of 2HG was only moderately elevated

335 in the amniotic fluids of Slc25a1 deficient mice albeit being higher in the brains, reaching only a five-
336 fold average enrichment compared to control (Fig. 8A,B). To then determine the relative enrichment
337 of the D- and L- enantiomer, a chiral derivatization method was employed (Cheng et al, 2015) (see
338 EV3A for the L/D peaks separation). We established that the D-enantiomer accounts for
339 approximately 70% of the total pool and represents the main pool enriched in *Slc25a1*$^{-/-}$ mice relative
340 to control (Fig. 8C,D). To further validate these results, we analyzed previously published data
341 derived from nine patients affected by D/L-2HGA (Pop et al, 2018; Prasun et al, 2015), and found a
342 comparable, albeit not esclusive prevalence of D-2HG (Fig. 8E). Importantly, in cells harboring wild-
343 type *IDH1/2* genes, the acute SLC25A1 knock-down (KD) led to a four to five fold accumulation of D-
344 2HG, again demonstrating that loss of SLC25A1 activity directly, but modestly induces enrichment of
345 this metabolite (Fig. 8F). To corroborate this important point, we also comparatively studied the
346 levels of D-2HG in fibrosarcoma cells, HT-1080, which harbor one of the most common *IDH1*
347 mutations, IDH1^{R132C}. This analysis confirmed the significantly lower enrichment of this enantiomer in
348 cells harboring the SLC25A1-KD relatively to cells expressing gain of function IDH1 mutants (Fig.
349 8G).
350
351 It is now emerging that wild-type IDH1/2 proteins can produce D-2HG, albeit at much lower rates and
352 concentrations (Ježek et al, 2020). First, we studied the IDH1 and IDH2 mRNA and proteins levels
353 and we determined that the expression of IDH1, but not of IDH2, was increased in the *Slc25a1*$^{-/-}$
354 MEFs and brains (Fig. 8H,I and EV3BC). Second, we employed inhibitors for IDH1 and 2 and studied
355 their effects on D-2HG accumulation. AG120 was initially developed as an inhibitor for mutant IDH1,
356 but more recently it was shown to have inhibitory activity at low concentrations against wild-type IDH1
357 in many cell lines (Zarei et al, 2022). As seen in Figure 8J, the accumulation of D-2HG was nearly
358 entirely suppressed by AG120, but not by the IDH2 inhibitor AGI-6780 (EV3D). Similarly to AG120,
359 the IDH1 shRNA led to a reduction of the D-2HG enantiomer in the patient derived cells, which also
360 over-expressed IDH1 (EV3E).
361

362 In the next set of experiments we directly explored the idea that low levels of 2HG can induce p53-
363 mediated OIS. To this end, we treated MEFs or primary human fibroblasts (HF) with 2HG. First, either
364 D- or L-2HG induced p53 and p21 (Fig. 8K). In addition, very low doses of either enantiomer (nM or
365 uM) induced SAβ-GAL (Fig. 8L-N). This effect did not increase when the concentrations were titrated
366 up to 1- to-10 mM (Fig. 8O), reflective of tumor concentrations, thus suggesting that induction of
367 senescence is a mechanism by which normal cells respond to low levels of 2HG. Further, treatment
368 with D-2HG induced pro-inflammatory SASPs typical IOS, but not of MiDAS, particularly IL-1β and IL-
369 6 (Fig.8P).
370
371 **Treatment of zebrafish embryos with 2HG partially recapitulates the phenotypes of SLC25A1**
372 **loss.** The effects of 2HG on embryonic development have only been studied directly in the two-cells
373 to blastocyst transition in murine embryos (Zhao et al, 2021). Given the predominant abundance of D-
374 2HG in D/L-2HGA sustained by SLC25A1 dysfunction, we first sought to explore directly its
375 contribution to embryonic development by using the zebrafish model as an experimental platform. By
376 performing dose-response experiments, we observed no overt toxicity at the concentrations used,
377 and we detected relevant phenotypes at concentrations ranging between 20-100 μM. The main organ
378 affected was the brain, which was small and bulging (Fig. 9A,B and quantified in 9C). Alterations in
379 the vertebral column and in the body curvature were also significant. In addition, many treated
380 embryos exhibited alterations in the size of the head, jaw and eyes, larger hearts as well as
381 pericardial edema. At an 80 μM D-2HG dose, embryos exhibited prominent disorganization of the
382 brain tissue (Fig. 9B). Given the concomitant presence of both D/L-2HG enantiomers we also
383 explored the effects of L-2HG alone or in combination with D-2HG, in this case at D/L ratio similar to
384 those observed previously and typical of D/L-2HGA. Specifically, low concentrations of L-2HG alone
385 induced a mild phenotype, which however became very severe at higher doses (Fig. 9D). The D-2HG
386 in combination with L-2HG induced a prominent cardiovascular phenotype consisting of heart
387 enlargement and reduced ability of the heart to pump blood (Fig. 9E and Supplemental Video 1).
Further, mixing D- and L at doses at which neither enantiomer alone induced severe alterations, 389
significantly worsened the phenotype (Fig. 9F), suggesting that the presence of both enantiomers in

390 SLC25A1-mediated D/L-2HGDH may worsen the phenotypical alterations. These phenotypes were
391 less prominent relatively to complete depletion of *slc25a1* with the targeted morpholino, which
392 resulted in relatively high percent of lethality (Catalina-Rodriguez et al, 2012). We conclude that
393 2HG at least partially contributes to the embryonic developmental alterations seen in D/L-2HGA
394 sustained by SLC25A1 deficiency.
395
396 **IOS and MiDAS co-operate to restrict growth in a p53-dependent fashion.** The qualitative
397 analysis of the SASP in the brains and in the *Slc25a1*$^{-/-}$ MEFs, showed a mixed pattern of
398 senescence involving pro-inflammatory signals derived from IOS, as well as SASPs typical of MiDAS.
399 We have partially dissected these events as we have shown that 2HG is, *per se*, able to induce the
400 inflammatory pro-oncogenic SASP arm, while enhanced glycolysis and decreased NAD^+ drive
401 mitochondrial dysfunction. In an attempt to reverse these senescence cues, we overexpressed the
402 cDNA encoding for the D-2HGDH clearing enzyme, D-2HGDH (see EV4A for the expression levels of
403 the protein). Overexpression of D-2HGDH reduced senescence in *Slc25a1*$^{-/-}$ MEFs (Fig. 10A).
404 Furthermore, treating *Slc25a1*$^{-/-}$ MEFs with either NMN (Fig. 10B) or with DCA (not shown), also
405 reduced the proportion of senescent cells. To determine the impact of these senescent programs on
406 proliferation, we performed colony forming assays in cells harboring the SLC25A1 knock-down. While
407 treatment with NMN or over-expression of D-2HGDH alone modestly influenced colony forming
408 ability, the combination had a more significant additive effect enhancing colony size and number
409 (Fig.10C and not shown). Importantly, this cooperative effect was specific for cells lacking SLC25A1
410 protein, as neither NMN or D2HGDH over-expression enhanced proliferation rates in the absence of
411 the SLC25A1-KD (EVBC). Hence, IOS and MiDAS act together to restrict growth in SLC25A1
412 deficient cells.
413
414 The OIS program serves as a fundamental tumor-suppressive mechanism, preventing cells that have
415 acquired proliferative capacity from progressing through the cell cycle *via* the activation of tumor
416 suppressors, including p53. However, cells eventually escape the senescent block by inactivating p53
417 and acquire the capapility to expand. First, we confirmed that the acute knockdown of SLC25A1 using

418 two distinct shRNAs enhanced p53 expression (Fig.10D). This result demonstrates that SLC25A1
419 depletion directly induces p53 and raises the question of whether such induction is responsible for the
420 proliferation defect of SLC25A1-deficient cells. To explore this concept, we employed a controlled
421 isogenic system, A549 cells, where the effects of the SLC25A1-KD were studied in the presence or
422 absence of the p53-KD again using colony forming assays. As shown in Figure 10E, we were able to
423 effectively achieve a double knock-down of both proteins. The results of these experiments clearly
424 demonstrated that the proliferation defect due to SLC25A1 depletion could be alleviated by
425 simultaneously knocking down p53, hence reinforcing the idea that elimination of p53 activity
426 ameliorates the proliferation defect imposed by dysfunctional SLC25A1 (Fig. 10F).
427
428
429
430
431
432
433
434
435
436
437
438
439
440
441
442
443
444
445

446 **DISCUSSION**

447 The pathogenesis of genetically inherited human diseases due to SLC25A1 loss is still largely
448 unclear. Using a multifaceted approach which includes a novel murine model of SLC25A1 deficiency
449 our results provide evidence that its inactivation leads to the engagement of two pathways of
450 senescence, OIS and MiDAS. They further show that accumulation of low doses 2HG and
451 mitochondrial dysfunction driven by enhanced glycolysis and depletion of NAD^+, respectively, trigger
452 these senescent programs leading to activation of the p53 (summarized in Fig. 10G). We have also
453 demonstated that the molecular and phenotypic alterations arising from SLC25A1 deficiency are in
454 part sustained by the accumulation of D-2HG based on the observation that in zebrafish, treatment
455 with this enantiomer was able to recapitulate some salient phenotypic features that overlap with the
456 *slc25a1* depletion induced by a specific morpholino. The main impact of these findings is in the
457 observation that SLC25A1 loss leads to only a modest enrichment of 2HG, yet these low
458 concentrations appear to be fully pathogenic. In addition, wild-type IDH1 is responsible for the
459 synthesis of the D-enantiomer at least in the model systems that we have studied. Finally, D-2HG
460 induces senescence, a finding only in apparent contrast with its definition of as "oncometabolite".
461 Indeed, our data suggest that the first time that the response of normal cells to low doses of 2HG is
462 the induction of senescence and that dismantling of downstream tumor suppressor pathways,
463 including p53, is necessary for transformation, similarly to oncogene induced senescence.
464

465 The above observations have several important implications. First, consistent with the RNAseq data
466 showing an enrichment of pro-oncogenic pathways, an important question is whether SLC25A1 loss
467 is eventually oncogenic. It is relevant to note that as in the case of VCFS and DGS, there is a link
468 between 2HG-acidurias and cancer risk. In fact, children affected by 2HG-acidurias sustained by
469 mutations of *IDH1/2* or *D/L-2HGDH*, exhibit high cancer incidence, particularly of oligodendriomas,
470 low grade gliomas, anaplastic astrocytomas and medulloblastomas (Murphey et al, 2022; Dilber et al,
471 2022; Srinivasan et al, 2020; Patay et al, 2012; Toer et al, 2017; Patay et al, 2015). The increased
472 cancer risk in D/L-2HGDA sustained by SLC25A1 dysfunction may be obscured by the early death
473 observed in these children, but deletions/mutations of the *SLC25A1* gene can be detected in various

474 tumors (unpublished observations). Second, it is well known that the presence of proto-oncogenes in
475 normal cells induces the activity of the p53 tumor suppressor to elicit senescence as a mechanism to
476 halt the proliferative capacity of cells that have acquired oncogenic potential. Our data now reveal that
477 2HG behaves as an oncogene, inducing p53/p21-mediated OIS senescence and thus, implying that
478 p53 interacts with potentially oncogenic metabolic products similarly to its interaction with oncogenic
479 proteins. This is a novel concept that will offer a paradigmatic example of how alterations in the
480 metabolism may lead to senescence and cancer. Third, our data have implications beyond diseases
481 linked to SLC25A1 deficiency. Low levels of enrichment of 2HG are currently considered non-
482 pathogenic, but this moiety is present in modest amount in metabolic disorders and in tumors that do
483 not harbor IDH1/2 mutations (Du and Hu, 2021). Our results challenge this concept, revealing
484 multifaceted mechanisms of action of 2HG depending on the cellular context, and as such, will likely
485 drive further investigations into the broader pathogenic role of this metabolite as well as of wild-type
486 *IDH1/2* genes in human diseases.
487
488 We have demonstrated that the IOS and MiDAS pathways are independently induced in cells lacking
489 SLC25A1 by discernible signals. Specifically, our previously published work had demonstrated that
490 this protein plays a fundamental role in maintaining the rates of mitochondrial respiration, as argued
491 not only based on the deletrious effects on OXPHOS of specific inhibitors for this protein (Fernandez
492 et al, 2020), but also given that over-expression of SLC25A1 enhances the rates of OXPHOS
493 (Palmieri et al, 2020; Jiang et al, 2017). The finding that SLC25A1 over-expression, *per se*, drives
494 mitochondrial oxidative metabolism, together with results presented herein, demonstrates that this
495 activity of SLC25A1 is independent of 2HG accumulation. The mechanisms by which SLC25A1 loss
496 leads to deterioration of OXPHOS were up to this point unclear, but we have now identified the
497 depletion of NAD^+ and high glycolytic rates, presumably due to the HIF1α-mediated pseudohypoxia
498 response, as at least in part responsible for this effect in the cellular models relevant to human
499 diseases that we have examined. It is also highly significant to note that the NAD^+-driven
500 pseudohypoxia response has been linked to aging (Gomes et al, 2013). Further, in the seminal work
501 of the Campisi's laboratory MiDAS was detected in murine models of progeroid syndromes (Wiley et

502 al, 2016). Indeed *Slc25a1* homozygous embryos exhibit growth retardation, wrinkled skin, and facial
503 deformities including anophtalmia, which are seen in models of progeria (Carrero et al, 2016). In
504 addition, deletion of the gene encoding for longevity associated deacetylase, *SIRT1* leads to
505 alterations similar to those seen in *Slc25a1*$^{-/-}$ mice, including the perinatal lethality, exencephaly, eye
506 abnormalities, small body size and the induction of p53-mediated senescence (Liu et a, 2012).
507 Interestingly, deficiencies of other mitochondrial transporters of the SLC25 family are known to lead to
508 mitochondrial dysfunction, early aging and progeroid features (Rodríguez-García et al, 2018; Writzl et
509 al, 2017). Viewed together with our findings, these observations raise the attractive possibility that the
510 MiDAS response in the context of SLC25A1 deficiency leads to an accelerated aging, progeroid
511 phenotype. The identification of drugs (DCA, NMN) able to reverse this deficit provides novel means
512 of therapeutic interventions.
513
514 In summary, data presented in this work reveal that complete elimination of SLC25A1-mediated
515 signaling during embryonic development leads to molecular and phenotypic alterations more complex
516 than anticipated and that disorders sustained by its loss should be reclassified as dismetabolic and
517 mitochondrial disorders. It is further relevant to note that the IOS and MiDAS pathways of senescence
518 have been considered distinct because of the nature of their up-stream regulatory signals and their
519 impact upon very different biological processes. Here, we identify SLC25A1 deficiency as a patho-
520 physiological context where these signals operate together. Lastly, we have observed an
521 enhancement of citrate-dependent pathways and lipid build-up in *Slc25a1* deficient embryos. Citrate
522 and lipids are well known mediators of inflammation and of senescence (Hong et al, 2023), raising the
523 question of whether a maladaptive compensatory response to replenish the cytosolic pool of citrate
524 and lipids also contribute to the loss of proliferative capacity. These conclusions notewistanding, it is
525 relevant to consider that the spectrum of molecular and biochemical alterations seen in *Slc25a1*$^{-/-}$
526 mice is global and various tissues might respond or adapt to SLC25A1 loss differently. Thus,
527 unraveling the complexity of tissue-specific functions of SLC25A1 will be an object of future
528 investigations. Though many of the pathological manifestations due to SLC25A1 deficiency are likely
529 irreversible, as they are acquired during embryogenesis and development, we predict that this study

530 will inform on therapeutic strategies able to ameliorate at least some aspects of these devastating
531 disorders.
532
533
534
535
536
537
538
539
540
541
542
543
544
545
546
547
548
549
550
551
552
553
554
555
556
557

558 **Methods**

559 **Study approval**. All animal studies were conducted in compliance with ethical regulations according
560 to protocol #2017-1192 approved by the Institutional Animal Care and Use Committee (IACUC) at
561 Georgetown University. All the mice were housed at Georgetown University Division of Comparative
562 Medicine, in a SPF vivarium which is maintained at a 12:12 h light:dark cycle, at 68–74°F and 30–
563 70% humidity range. Mice were euthanized according to the IACUC guidelines and approved
564 protocols.

565 **Cell culture**

566 The A549 and H1299 cell line were obtained from the tissue culture core facility at LCCC. Cells were
567 grown in Dulbecco's Modified Eagle's Medium (DMEM 4500 mg/L glucose) supplemented with 10%
568 fetal bovine serum, 4 mM L-glutamine, 1 mM sodium pyruvate and 1% antibiotic solution. The
569 S*LC25A1*-specific shRNA vectors were purchased from Sigma (TRCN0000232825;
570 TRCN0000255350) and validated before (6,18,24). Octyl-2-HG (Cayman 16366, 16367) was diluted
571 in PBS pH 7.2.

572 **Mice**

573 The S*lc25a1* heterozygous mice were purchased from the Mutant Mouse Resource Research Center
574 (MMRRC) (C57BL/6N-*Slc25a1*$^{tm1a(EUCOMM)Wtsi}$, RRID:MMRRC_042258-UCD). The targeting vector
575 allows for constitutive or conditional deletion of the *SLC25A1* gene through the incorporation of an
576 *IRES:lacZ* trapping cassette which is inserted between introns 1 and 5 of the *Slc25a1* gene [24]. Mice
577 were maintained on a 12h light/dark cycle and were supplied with food and water ad libitum. To
578 obtain mouse lacking *Slc25a1* we crossed heterozygous *Slc25a1*$^{+/-}$ heterozygous mice. Pregnancy
579 was confirmed by checking for vaginal plugs and the increase in body weight measured weekly.

580 **Embryos, brains and amniotic fluids collection**

581 Pregnant mice were euthanized at different stages of pregnancy and whole embryos were collected.
582 Typically, embryos were harvested at E9.5-E19, and tips of tails were collected for genotyping. For
583 IHC, embryos were fixed in 4% paraformaldehyde overnight, transferred to 80% EtOH and sent for
584 histological processing. Paraffin embedding, sectioning and hematoxylin/eosin staining of embryos
585 tissue sections were performed by Histology and Microscopy Core of Georgetown University or by

586 VitroVivo Biotech. To collect the amniotic fluid, and avoid cross-contamination, we typically selected
587 embryos distally located. After transferring the embryos to a clean dish, the amniotic fluid was
588 collected by 1-mL syringe and 27-gauge needle. For biochemical and molecular analysis, indicated
589 organs were dissected, quickly washed in PBS and snap frozen in liquid nitrogen. For the collection of
590 the brains, skin and skull (when present) were carefully removed. The isolated brains were quickly
591 washed in PBS twice, snap frozen in liquid nitrogen and stored at -80°C until processed for further
592 analyses.

593 **CT Images acquisition from the International Mouse Phenotyping Consortium**.

594 The IMPC has provided CT images of *slc25a1*$^{-/-}$ mice without description of the phenotypes. Analysis
595 of these images and phenotype identification was performed in house at GUMC through the help of
596 the Preclinical Imaging Research Laboratory (PIRL) facility.

597 **2HG quantification with LC/MS/MS and GS/MS/MS**

598 For LC/MS a targeted metabolomics method was used to quantitate 2-HG using QTRAP® 7500 LC-
599 MS/MS System (Sciex, MA, USA). The 2HG standard was from Sigma Aldrich (# 90790-10MG). For
600 the purpose, 75 µL of extraction buffer (methanol/water 50/50) containing 200 ng/mL of 4-nitrobenzoic
601 acid as internal standard for negative mode was added to the cell pellet and sample tube was
602 plunged into dry ice for 30 sec and 37 °C water bath for 90 sec. This cycle was repeated for two more
603 times and then samples were sonicated for 1 minute. The samples were vortexed for 1 min and kept
604 on ice for 20 minutes followed by addition of 75 µL of ACN. The samples were incubated at -20 °C for
605 20 minutes for protein precipitation. The samples were centrifuged at 13,000 rpm for 20 minutes at 4
606 °C. The supernatant was transferred to MS vial for LC-MS analysis. 20 µL of each prepared sample
607 was mixed to generate the pooled QC sample. For GC-TOF amniotic fluids or tissue samples were
608 processed using 500 µL of 50% methanol in water containing the internal standard (4-Nitrobenzoic
609 acid, prepared in MeOH at a concentration of 20 µg/mL). The samples were homogenized on ice to
610 ensure tissue lysis and metabolite extraction was then vortexed for 2 minutes. A volume of 10 µL was
611 withdrawn from the homogenized tissue suspension for the protein quantification assays. The
612 samples were vortexed for 2 minutes and left for 2 hours at room temperature. The BCA kit used for
613 the protein quantification assay was Pierce™ BCA Protein Assay Kit (Cat # 23225). A volume of 20

614 µL of methoxyamine (20 mg/mL) was added to the dried tissue extracts and then heated in an
615 agitator at 60 °C for 30 minutes. This was followed by 100 µL of MSTFA. The vials were transferred to
616 an agitator to heat at 60 °C for 30 more minutes. Finally, the vials were capped and a volume of 1.5
617 µL was injected directly to the GC-MS. The samples were allowed to react at room temperature for 20
618 minutes before being transferred to the GC for injection. Briefly after the derivatization process, a
619 volume of 1.5 µL of the derivatized solution was injected in (1:10) split mode into an Agilent 7890B
620 GC system (Santa Clara, CA, USA) that was coupled with a Pegasus HT TOF-MS (LECO
621 Corporation, St. Joseph, MI, USA). Separation was achieved on a Rtx-5 w/Integra-Guard capillary
622 column (30 m x 0.25 mm ID, 0.25 µm film thickness; Restek Corporation, Bellefonte, PA, USA), with
623 helium as the carrier gas at a constant flow rate of 0.9 mL/min. The temperature of injection, transfer
624 interface, and ion source were set to 150, 270, and 320 °C, respectively. The GC temperature
625 programming was set to 0.2 minutes of isothermal heating at 70 °C, followed by 6 °C/min oven
626 temperature ramping to 270 °C, a 7.0 minute isothermal heating of 270 °C, 20 °C/min to 320 °C, and
627 a 2.0 min. isothermal heating of 320 °C. Electron impact ionization (70 eV) at full scan mode (40–600
628 *m*/*z*) was used, with an acquisition rate of 20 spectra per second in the TOF/MS setting.

629 **Metabolomic and Lipidomics**

630 Metabolomic (targeted and untargeted was performed as described before (Tan et al, 2020). The
631 lipidomic method used in the brains of *Slc25a1*$^{-/-}$ mice, is designed to measure 19 classes of lipid
632 molecules which includes diacylglycerols (DAG), chloesterol esters (CE), sphingomyelins (SM),
633 phosphtatidylchloine (PC), triacylglycerols (TAG), free fatty acids (FFA), ceramides (CE),
634 dihydroceramides (DCER), hexosylceramide (HCER), lactosylceramide (LCER),
635 phosphatidylethanolamine (PE), lysophosphtatidylchloine (LPC), lysophosphatidylethnolamine
636 (LPE),phosphatidic acid (PA), lysophosphatidic acid (LPA), phosphatidylinositol (PI),
637 lysophosphotidylinositol (LPI), phosphatidylglycerol (PG) and phosphatidylserine (PS) using QTRAP®
638 5500 LC-MS/MS System (Sciex). For the purpose, 20 µL of each amniotic fluid sample was dissolved
639 in 100 µL of chilled isopropanol containing internal standards was added and samples were vortexed.
640 The samples were vortexed again for 1 min and kept on ice for 30 minutes. Samples were incubated
641 at -20 °C for 2 hours for complete protein precipitation. The samples were centrifuged at 13,000 rpm

642 for 20 minutes at 4 °C. The supernatant was transferred to MS vial for LC-MS analysis. Five µL of
643 each sample was injected onto a Xbridge amide 3.5 µm, 4.6 X 100 mm (waters) using SIL-30 AC
644 auto sampler (Shimazdu) connected with a high flow LC-30AD solvent delivery unit (Shimazdu) and
645 CBM-20A communication bus module (Shimazdu) online with QTRAP 5500 (Sciex, MA, USA)
646 operating in positive and negative ion mode. Obtained results were analyzed using MetaboAnalyst.

647 **Brain TCA cycle analyses**

648 Tissue samples were mixed with 400 µL of MeOH containing the internal standard (4-Nitrobenzoic
649 acid) which was prepared in MeOH at a concentration of 30 µg/mL and homogenized for 60 seconds.
650 A volume of 10 µL was withdrawn from the tissue suspension for the protein concentration assay. The
651 samples were mixed for 2 minutes, left at -20 °C. for 2 hours then centrifuged for 30 min at a speed of
652 16,000 X g and a temperature of 4 °C. The supernatant was separated and transferred to the GC
653 vials then dried under vacuum at room temperature. Samples were derivatized and injected into
654 GCMS instrument. Protein concentration was determined using BCA assay. The Briefly after the
655 derivatization process, a volume of 2.0 µL of the derivatized solution was injected in a splitless mode
656 into an Agilent 7890B GC system (Santa Clara, CA, USA) that was coupled with a Pegasus HT TOF-
657 MS (LECO Corporation, St. Joseph, MI, USA). Separation was achieved on a Rtx-5 w/Integra-Guard
658 capillary column (30 m x 0.25 mm ID, 0.25 µm film thickness; Restek Corporation, Bellefonte, PA,
659 USA), with helium as the carrier gas at a constant flow rate of 0.8 mL/min. The temperature of
660 injection, transfer interface, and ion source was set to 150, 270, and 320 °C, respectively. The GC
661 temperature programming was set to 0.2 min. of isothermal heating at 70 °C, followed by 6 °C/min
662 oven temperature ramping to 300 °C, a 1.0 min. isothermal heating of 300 °C, 20 ° C/min to 320 °C,
663 and a 2.0 min. isothermal heating of 320 °C. Electron impact ionization (70 eV) at full scan mode (40–
664 600 m/z) was used, with an acquisition rate of 20 spectra per second in the TOF/MS setting.

665 **Genotyping**

666 Mouse tail biopsies and agarose gel electrophoresis was used for analysis of PCR products. The
667 PCR conditions used were as follows: 94 °C for 1 minute, 5 cycles at 94 °C for 30 s, 63 °C for 40s, 68
668 °C for 1 min; followed by 30 cycles (94 °C for 30 seconds, 55 °C for 40 seconds, and 72 °C for 1 min),

669 72 °C for 7 min then kept in 4 °C before use. The primers used for genotyping are indicated in EV
670 Table 1.

671 **Mouse embryonic fibroblasts isolation**

672 Freshly dissected embryos at E10-E14 were used for isolation of mouse embryonic fibroblasts
673 (MEFs). Brain, liver, internal organs and tail were removed, and the remaining tissues were rinsed
674 with PBS and transferred to a 10 cm plate. Embryos were then minced with a sterile razor blade in
675 the presence of TrypLE™ Express Enzyme (Gibco™, 12604021) following by 10 min incubation on a
676 shaker at RT. Finally, the cells were pipetted multiple times to further disintegrate the tissue, and then
677 the freshly isolated cell were cultured in high glucose DMEM medium (Dulbecco's Modified Eagle
678 Medium with 10% fetal bovine serum, 4500 mg/L glucose, 4 mM L-glutamine, 1 mM sodium pyruvate
679 and 1% antibiotic solution).

680 **Protein analysis and immunoblot**

681 Proteins from cells or frozen tissue samples, grinded in liquid nitrogen, were homogenized in RIPA
682 buffer supplemented with cOmplete Mini Protease Inhibitor Tablets (Roche, 11836153001). Protein
683 quantification was done by using Coomassie (Bradford) Protein Assay Kit (Pierce). Equal amount of
684 protein lysate was loaded and separated in an SDS-polyacrylamide gel electrophoresis using
685 Novex™ 4-20% Tris-Glycine Mini Gel (Invitrogen, XP04200PK2) and transferred to PVDF membrane
686 (Millipore, IPVH304F0). The membrane was blocked in blocking buffer with 10% horse serum to
687 prevent non-specific binding, followed by incubation with different antibodies: SLC25A1 (Santa Cruz,
688 sc-86392 or Proteintech, 15235-1-AP), ACC1 (Cell Signaling, #3676), FASN (Cell Signaling, #3180),
689 IDH1 (Proteintech, 12332-1-AP), AMPK-α (Cell Signaling, #5832), pAMPK-α (Cell Signaling, #2535),
690 Chk1 (Cell Signaling, Cat#2360), HIF1-alpha (Novus Biological, Cat#NB100-105), p21 Waf1/Cip1
691 (Cell Signaling, #37543), mTOR (Cell Signaling, #2983), pH2A.X (Cell Signaling, #9718), p53 (Santa
692 Cruz, sc-126 and Sigma Aldrich, OP29-100UG), D2HGDH (Proteintech, 13895-1-AP). Appropriate
693 horseradish peroxidase–conjugated secondary antibody (Invitrogen) was applied after incubation with
694 primary antibody, SuperSignal™ West Pico PLUS Chemiluminescent Substrate (Thermo Scientific,
695 34577) or SuperSignal™ West Dura Extended Duration Substrate (Thermo Scientific, 34075) were

696 used for protein detection. β-Actin (Santa Cruz, sc-47778) and HSP70 (Santa Cruz, sc-24) served as
697 a loading control.

698 **Quantitative real-time PCR**

699 Total RNA was extracted from frozen tissue and cells pellet samples using TRIzol™ Reagent
700 (Invitrogen, 15596026), followed by RNA quantification with NanoDrop (Implen, Munich, Germany).
701 After genomic DNA treatment by DNase I (Invitrogen, AM2222), total RNA was used in cDNA
702 synthesis with SuperScript™ IV Reverse Transcriptase (Invitrogen, 18090200) and random hexamers
703 according to the manufacturer's instructions. The quantitative Reverse Transcriptase-PCR (qRT-
704 PCR) was performed on the QuantStudio™ 12K Flex Real-Time PCR System (Applied Biosystems)
705 with PowerUp™ SYBR Green Master Mix (Applied Biosystems). The obtained results were
706 normalized to housekeeping genes, and their sequences will be provided.

707 **RNA sequencing**

708 Brains isolated from 18.5 dpf embryos were used for RNA sequencing. Briefly, RNA isolatation and
709 RNA sequencing (RNAseq) was performed by Novogene. Raw intensity data was background
710 corrected and filtered of low expression genes across samples (low expression genes across
711 samples (low expression genes across samples (<100 read) prior to analysis. Normalization and
712 differential expression were performed in R using the DESeq2 package. A cutoff of $p < 0.05$ and $|FC|$
713 > 2 were used to determine differentially expressed genes. The GSEA Java-based software package
714 from The Broad Institute was used to identify top enriched pathways in *Slc25a1*$^{+/+}$ and *Slc25a1*$^{-/-}$
715 brains. Reference genome and gene model annotation files were downloaded from genome website
716 directly. Index of the reference genome was built using Hisat2 v2.0.5 and paired-end clean reads
717 were aligned to the reference genome using Hisat2 v2.0.5. featureCounts v1.5.0-p3 was used to
718 count the reads numbers mapped to each gene. FPKM of each gene was calculated based on the
719 length of the gene and reads countmapped to this gene. FPKM, expected number of Fragments Per
720 Kilobase of transcript sequence per Millions base pairs sequenced, considers the effect of
721 sequencing depth and gene length for the reads count at the same time, and is currently the most
722 commonly used method for estimating gene expression levels. Differential expression analysis was
723 performed using the DESeq2 R package (1.20.0). The P values were adjusted using the Benjamini &

724 Hochberg method. Corrected P-value of 0.05 and absolute fold change of 2 were set as the threshold
725 for significantly differential expression. Enrichment analysis of differentially expressed genes.

726 **Immunohistochemistry and immunofluorescence**

727 Age-matched embryos were removed from the uteri and fixed in 4% paraformaldehyde in phosphate-
728 buffered saline and paraffin embedded, sectioned in the mid sagittal plane and stained with
729 hematoxylin and eosin (H&E) and anti-Slc25a1 antibody (Proteintech, 15235-1-AP), used at 1/150
730 dilution. Consecutive sections with the primary antibody omitted were used as negative controls.
731 Stained slides were scanned using the VS120 Virtual Slide Microscope (Olympus). For
732 immunofluorescence (IF) staining, FFPE embryo sections were deparaffinized and sodium citrate was
733 used for antigen retrieval. Slides were washed in PBS, blocked using TBST+20% Aquablock, and
734 incubated with primary antibodies: anti-Slc25a1 (Proteintech, 15235-1-AP) and p21 (Santa Cruz, sc-
735 756). Finally, samples were washed in PBST and incubated with appropriate secondary antibody and
736 DAPI or Hoechst (Sigma-Aldrich). IF samples were acquired using a Zeiss LSM800 laser scanning
737 confocal microscope and analyzed using ImageJ/Fiji software.

738 **Electron microscopy**

739 Pregnant females were euthanized and perfused with 2.5% glutaraldehyde and 2% PFA in 0.15M
740 cacodylate buffer. Following osmication, dehydration, and embedding in Epon 814, embryos heads
741 were sectioned transversely (at the midpoint) at 120 nm using an ultramicrotome. Ultrathin sections
742 were placed in silicon wafers and carbon taped in aluminum stubs for scanning electron microscopy
743 (SEM) imaging in a Helios NanoLab 660 dual beam microscope. To maximize the collection of the
744 backscattered electrons and produced TEM-like images, a high contrast solid-state backscatter
745 electron detector, in magnetic immersion mode and 4 μm working distance, was used. The
746 acquisition was performed using 2 kV and 0.40 nA as the current landing. Overview images including
747 the entire section were taken at a magnification of 5,000× and analyzed using ImageJ software.

748 **Senescence-associated β-Gal staining**

749 Cells grown on a 6-well plate were washed with PBS, fixed with fixative solution and stained with x-
750 gal according to the manufacturer protocol (Cell Signaling, #9860). After counterstaining with DAPI,

751 cells were imaged using an Olympus IX-71 Inverted Epifluorescence Scope and multiple images of
752 each well were taken for quantification.

753 **Colony formation assay**

754 H1299 and p53H1299 (or indicated cells) were plated in a six-well plate at density 500 cells/well for
755 14 days, and the medium was replaced every 3 days. Additionally, indicates cells were treated
with 756 nicotinamide mononucleotide (NMN, Selleckchem, catalog No.S5259) 24h after plating for 13
days, 757 and the medium was replaced every 3 days. Cells were fixed in 4% paraformaldehyde,
stained with 758 crystal violet and imaged/photographed to visualize the results. Quantification was
done by manual 759 counting and measuring stained area with image J.

760 **Lentivirus production and infection**

761 Control empty vector and vector shIDH1 were purchased from Sigma. Lentiviruses were produced in
762 Lenti-X 293T cells with Third Generation Packaging Mix (Applied Biological Materials Inc.,
763 Cat#LV053) according to the manufactureser's instruction. Cells were transduced with lentiviruses
764 and Polybrene Infection/Transfection Reagent (Millipore) reagents for 24 hrs and 0.5 μg/ml puromycin
765 was used to obtain stably expressing cell lines.

766 **D2HGDH overexpression (Plasmids and transfection)**

767 D2HGDH expression plasmid (OriGene, RC207367) and pRc/CMV expression plasmid (Invitrogen)
768 were used. Cells were plated in a six-well plates and allowed to grow overnight, and transfected using
769 Lipofectamine 2000 (Invitrogen, cat. 11668-030) and OPTI-MEM reduced serum media (Gibco, cat.
770 31985-062). The medium was replaced after 24 h. The D2HGDH overexpression was verified by
771 Western blotting using D2HGDH antibody (Proteintech, 13895-1-AP).

772 **Seahorse extracellular flux analyzer measurements**

773 Cells were seeded at 10 000 cells/well density in high glucose DMEM with 10% FBS, 1 mM pyruvate
774 and 1% antibiotic solution, and the following day treated with the indicated drug/vehicle for 24 h.
775 Seahorse measurements were done according to the manufacturer's instructions. Briefly: for the
776 mitochondrial stress test, the medium was replaced with DMEM without FBS or bicarbonate,
777 containing 5 or 10 mM glucose, 1 mM pyruvate, 2 mM glutamine and placed in a CO2 free incubator
778 at 37 °C for 1 h, transferred to the Xf96 extracellular flux analyzer (Agilent). The program consisted of

779 three measurements of OCR/ECAR before the injection of each drug: oligomycin (0.5 μM final
780 concentration), FCCP (2 μM) and rotenone/antimycin (0.5 μM of each).
781 **ETC Respiratory Complex activities**. The activities of the ETC were assessed with the Seahorse
782 analyzer with injections to study individual complexes as follows. For complex I after mild
783 permeabilization, injection 1: Pyruvate 10mM, Malate 5mM; injection 2: Rotenone. For complex II:
784 injection 1: Rotenone (to inhibit complex I), injection 2: Succinate (10mM), Injection 3: Atpenin A5
785 (complex II inhibitor). For complex III: injection 1: pyruvate 10mM, injection 2: antimycin. For complex
786 IV:injection 1: pyruvate 10mM injection 2: sodium Azide (200uM). ATP synthase: injection 1: pyruvate
787 10mM, injection 2: oligomycin.
788 **2HG analysis**
789 The α-Hydroxyglutaric Acid was obtained from Cayman Chemicals. Diacetyl-L-tartaric anhydride
790 (DATAN) was purchased from FisherScientific. All other reagents and solvents were of analytical and
791 LCMS grade. Sample preparation: a volume of 50 μL from amniotic fluid was extracted with 250 μL of
792 methanol containing 0.004 mmol/L of the internal standard (IS). Cell pellets were extracted with a
793 volume of 1 mL of methanol containing 0.004 mmol/L of the internal standard. Samples were
794 centrifuged for 20 minutes at 14, 000 X g and 4 °C. The supernatant was separated in a clean set of
795 vials. The vial contents were evaporated to dryness at 22 °C by a gentle flow of nitrogen. The di-
796 acetyltartaryl derivative was prepared by treating the dry residue with 50 μL of freshly made 50
797 mg/mL DATAN in Acetonitrile–acetic acid (4:1 by volume). The vials were capped and heated at 75
798 °C for 60 minutes. After the vial were cooled to room temperature, the mixture was evaporated to
799 dryness by a nitrogen stream at room temperature, the residue was redissolved in 100 μL of distilled
800 water, and 10 μL of the aqueous solution was injected on the LC column and analyzed by LCMS. The
801 sample, prepared in the first step, were analyzed on a Sciex QTRAP 4500 mass spectrometer
802 equipped with a Shimadzu Prominence UFLC XR System whereas, it was separated Phenomenex
803 Lux 3 μm AMP, LC Column 150 x 3.0 mm, PN: 00F-4751-Y0. The column temperature was kept at 22
804 0C. Solvent A was 100% LCMS grade water with 0.1% formic acid and solvent B was 100% LCMS
805 grade acetonitrile with 0.1% formic acid. The source temperature was kept at kept at 220 0C. The ion
806 spray voltage was -4500 volts. The flow rate was consent throughout the method and was set to 0.3

807 mL/min. The mass spectrometry method was set to a Negative MRM mode with a cycle time of 0.99
808 second. The targeted masses of the derivatized 2-HG were m/z 363, 147, and 129 Da. The Entrance
809 Potential (EP) was set to -10 volts and the Declustering Potential (DP), the Collision Cell Exit
810 Potential (CXP) were set to values optimized previously for each and every assigned transition. The
811 concentration of the analyte in urine was calculated by interpolation of the observed analyte/IS peak-
812 area ratio based on the linear regression line for the calibration curve, which was obtained by plotting
813 peak-area ratios vs analyte concentration. Data was analyzed using Analyst 1.7 and Sciex OS
814 software for quantification.

815 **D/L-2HG Derivatization method**

816 The α-Hydroxyglutaric Acid was obtained from Cayman Chemicals. Diacetyl-L-tartaric anhydride
817 (DATAN) was purchased from FisherScientific. All other reagents and solvents were of analytical and
818 LCMS grade. A volume of 50 µL from amniotic fluid was extracted with 250 µL of methanol containing
819 0.004 mmol/L of the internal standard (IS). Cell pellets were extracted with a volume of 1 mL of
820 methanol containing 0.004 mmol/L of the internal standard. Samples were centrifuged for 20 minutes
821 at 14, 000 X g and 4 °C. The supernatant was separated in a clean set of vials. The vial contents
822 were evaporated to dryness at 22 °C by a gentle flow of nitrogen. The di-acetyltartaryl derivative was
823 prepared by treating the dry residue with 50 µL of freshly made 50 mg/mL DATAN in Acetonitrile–
824 acetic acid (4:1 by volume). The vials were capped and heated at 75 °C for 60 minutes. After the vial
825 were cooled to room temperature, the mixture was evaporated to dryness by a nitrogen stream at
826 room temperature, the residue was redissolved in 100 µL of distilled water, and 10 µL of the aqueous
827 solution was injected on the LC column and analyzed by LCMS. The sample, prepared in the first
828 step, were analyzed on a Sciex QTRAP 4500 mass spectrometer equipped with a Shimadzu
829 Prominence UFLC XR System whereas, it was separated Phenomenex Lux 3 µm AMP, LC Column
830 150 x 3.0 mm, PN: 00F-4751-Y0. The column temperature was kept at 22 0C. Solvent A was 100%
831 LCMS grade water with 0.1% formic acid and solvent B was 100% LCMS grade acetonitrile with 0.1%
832 formic acid. The source temperature was kept at kept at 220 0C. The ion spray voltage was -4500
833 volts. The flow rate was consent throughout the method and was set to 0.3 mL/min. The mass
834 spectrometry method was set to a Negative MRM mode with a cycle time of 0.99 second. The

835 targeted masses of the derivatized 2-HG were m/z 363, 147, and 129 Da. The Entrance Potential
836 (EP) was set to -10 volts and the Declustering Potential (DP), the Collision Cell Exit Potential (CXP)
837 were set to values optimized previously for each and every assigned transition. The concentration of
838 the analyte in urine was calculated by interpolation of the observed analyte/IS peak-area ratio based
839 on the linear regression line for the calibration curve, which was obtained by plotting peak-area ratios
840 vs analyte concentration. Data was analyzed using Analyst 1.7 and Sciex OS software for
841 quantification.

842 **Zebrafish**

843 All zebrafish procedures were performed in accordance with NIH guidelines for the maintenance and
844 use of laboratory animals and approved by the Georgetown University Institutional Animal Care and
845 Use Committee Protocol #2017-0078. Mixed wild-type, or *mitfa*$^{w2/w2}$*; mpv17* $^{a9/a9}$ (casper), embryos were
846 obtained by pair-wise and group breeding, and raised in fish water (0.3 g/L sea salts) at 28°C. For
847 drug treatments, (2R)-Octyl-〈-hydroxyglutarate (Cayman Chemicals) and (2S)-Octyl-〈-
848 hydroxyglutarate (Cayman Chemicals), solutions were prepared in fish water. Embryos were treated
849 at blastula, 1 dpf, or 2 dpf stages at a density of 100ul drug solution per embryo. Chorions were
850 removed at 1 dpf by 10 min incubation in 200ug/ml pronase. Drug solutions were replaced daily. SA–
851 β–GAL staining was performed as described (Da Silva-Álvarez et al., 2020) modified with the
852 replacement of X-gal with Bluo-Gal, 5-Bromo-3-indolyl β-D-galactopyranoside.

853 **Statistical analyses**

854 For the analysis of the RNAseq experiments in the brain, differentially Expressed Genes were
855 obtained using DESeq2 (2). Significantly upregulated Genes (FDR < 0.05) were assessed for
856 pathway enrichment using the Reactome 2022 database (5) via EnrichR (4). Significantly enriched
857 Pathways were clustered via GeneSetCluster(3) using a distance score that reflects similarities in
858 genes mapping to multiple significantly enriched pathways. Similar processes were summarized by
859 secondary annotation. The p-values of Reactome pathway enrichment were displayed as a Heatmap
860 via GraphPad Prism. For all experiments, results are presented as mean value ±SD or SEM, unless
861 specified otherwise. Statistical significance was assessed using unpaired non parametric t-test,

862 unless indicated otherwise. Significant differences were graphed using GraphPad Prism software and
863 $p < 0.05$ was considered as statistically significant.
864
865 **Data availability.** All data will be made available on public databases and upon request.
866
867 **Authors contribution.** MLA designed all experiments and wrote the paper. JV accrued the patients
868 derived cell lines from patients under his care. AKP performed the majority of the experiments,
869 organized the data for the Figures and proof-edited the manuscript for accuracy in the description of
870 the experiments. MT generated the mouse colonies and worked with AKP for three years on this
871 project. RR performed the IHC and the IF experiments. AMI designed and performed the statistical
872 analyses on the transcriptomic data. HF performed the Seahorse experiments in the *Slc25a1*$^{-/-}$ MEFs
873 and contributed to the initial functional characterization of the mice-derived cells. RM has maintained
874 all the mouse strains during Covid 19, and performed several experiments. GWP provided
875 supervision to RR with the IF experiments. EG and MLA designed the experiments in zebrafish, EG
876 performed the experiments, assembled the Figures and provided interpretation of the results. CA
877 provided expertise in the interpretation of the phenotype and of the CT scans of the mice, proof-
878 edited the manuscript and offered inputs on this project throughout the years.
879
880 **Declaration of Competing Interest.** The authors declare that they have no known competing
881 financial interests or personal relationships that could have appeared to influence the work reported in
882 this paper.
883
884 **Acknowledgements.** Studies on SLC25A1 in the MLA lab have been supported by R01CA193698,
885 R21DE028670 and R21CA256546. JV is the Cleveland Family Endowed Chair in Pediatric Research
886 with support in part from NIH grant R01DK109907. All these studies have been supported by the
887 outstanding facility at GUMC and by the 2P30CA051008-30 CCSG grant. We are grateful to Dr.
888 Anton Wellstein for many inputs on this project, to the Riegel/Wellstein and to Dr. Chunling Yi
889 laboratories for sharing reagents and instrumentation. We thank Drs. Michael Girgis and Amrita

Cheema for the outstanding contributions for the metabolomic analyses and for the derivatization of D/L-2HG. We are also very grateful to Anastas Popratiloff and Cheryl Clarkson for the ECM analysis and to Lawrence F. Kroemer for initial aid with the assessment of the brain alterations in the mice. We thank Sarah Flowers for her inputs on all of the projects related to SCL25A1.

938
939 **References**

940 Carrero D, Soria-Valles C, López-Otín C (2016) Hallmarks of progeroid syndromes: lessons
941 from mice and reprogrammed cells. *Dis Model Mech* 9: 719-735

942 Catalina-Rodriguez O, Kolukula VK, Tomita Y, Preet A, Palmieri F, Wellstein A, Byers S,
943 Giaccia AJ, Glasgow E, Albanese C, Avantaggiati ML (2012) The mitochondrial citrate transporter,
944 CIC, is essential for mitochondrial homeostasis. *Oncotarget* 3: 1220-1235

945 Chaouch A, Porcelli V, Cox D, Edvardson S, Scarcia P, De Grassi A, Pierri CL, Cossins J,
946 Laval SH, Griffin H, et al (2014) Mutations in the Mitochondrial Citrate Carrier SLC25A1 are
947 Associated with Impaired Neuromuscular Transmission. *J Neuromuscul Dis* 1: 75-90

948 Cheng QY, Xiong J, Huang W, Ma Q, Ci W, Feng YQ, Yuan BF (2015) Sensitive
949 Determination of Onco-metabolites of D- and L-2-hydroxyglutarate Enantiomers by Chiral
950 Derivatization Combined with Liquid Chromatography/Mass Spectrometry Analysis. *Sci Rep* 5: 15217

951 Cohen I, Staretz-Chacham O, Wormser O, Perez Y, Saada A, Kadir R, Birk OS (2018) A
952 novel homozygous SLC25A1 mutation with impaired mitochondrial complex V: Possible phenotypic
953 expansion. *Am J Med Genet A* 176: 330-336

954 Cuollo L, Antonangeli F, Santoni A, Soriani A (2020) The Senescence-Associated Secretory
955 Phenotype (SASP) in the Challenging Future of Cancer Therapy and Age-Related Diseases. *Biology*
956 *(Basel)* 9: 485

957 de Klein N, Tsai EA, Vochteloo M, Baird D, Huang Y, Chen CY, van Dam S, Oelen R, Deelen
958 P, Bakker OB, et al (2023) Brain expression quantitative trait locus and network analyses reveal
959 downstream effects and putative drivers for brain-related diseases. *Nat Genet* 55(3): 377-388

960 Dickinson ME, Flenniken AM, Ji X, Teboul L, Wong MD, White JK, Meehan TF, Weninger WJ,
961 Westerberg H, Adissu H, Baker CN, et al (2016) High-throughput discovery of novel developmental
962 phenotypes. *Nature* 537: 508-514

963 Dilber B, Havalı C, Eroglu N, Aydın K, Şahin S, Cansu A (2020) Cerebral neoplasm in L-2-
964 hydroxyglutaric aciduria: two different presentations. Childs Nerv Syst 36: 1545-1548

965 Du X, Hu H (2021) The Roles of 2-Hydroxyglutarate. *Front Cell Dev Biol* 9: 651317

966 Edvardson S, Porcelli V, Jalas C, Soiferman D, Kellner Y, Shaag A, Korman SH, Pierri CL,
967 Scarcia P, Fraenkel ND, et al (2013) Agenesis of corpus callosum and optic nerve hypoplasia due to
968 mutations in SLC25A1 encoding the mitochondrial citrate transporter. *J Med Genet* 50: 240-245
969 Fernandez HR, Gadre SM, Tan M, Graham GT, Mosaoa R, Ongkeko MS, Kim KA, Riggins
970 RB, Parasido E, Petrini I, et al (2018) The mitochondrial citrate carrier, SLC25A1, drives stemness
971 and therapy resistance in non-small cell lung cancer. *Cell Death Differ* 25: 1239-1258
972 Funato N (2022) Craniofacial Phenotypes and Genetics of DiGeorge Syndrome. *J Dev Biol*
973 10: 18
974 Gomes AP, Price NL, Ling AJ, Moslehi JJ, Montgomery MK, Rajman L, White JP, Teodoro JS,
975 Wrann CD, Hubbard BP, et al (2013) Declining NAD(+) induces a pseudohypoxic state disrupting
976 nuclear-mitochondrial communication during aging. *Cell* 155(7):1624-38
977 Groza T, Gomez FL, Mashhadi HH, Muñoz-Fuentes V, Gunes O, Wilson R, Cacheiro P, Frost
978 A, Keskivali-Bond P, Vardal B, et al (2023) The International Mouse Phenotyping Consortium:
979 comprehensive knockout phenotyping underpinning the study of human disease. *Nucleic Acids Res*
980 51: D1038-D1045
981 Hirata M, Sasaki M, Cairns RA, Inoue S, Puviindran V, Li WY, Snow BE, Jones LD, Wei Q,
982 Sato S, et al (2015) Mutant IDH is sufficient to initiate enchondromatosis in mice. *Proc Natl Acad Sci*
983 *U S A* 112: 2829-2834
984 Hong JR, Jin L, Zhang CY, Zhong WJ, Yang HH, Wang GM, Ma SC, Guan CX, Li Q, Zhou Y
985 (2023) Mitochondrial citrate accumulation triggers senescence of alveolar epithelial cells contributing
986 to pulmonary fibrosis in mice. *Heliyon* 9(6):e17361
987 Ježek P (2020) 2-Hydroxyglutarate in Cancer Cells. *Antioxid Redox Signal* 33: 903-926
988 Jiang L, Boufersaoui A, Yang C, Ko B, Rakheja D, Guevara G, Hu Z, DeBerardinis RJ (2017)
989 Quantitative metabolic flux analysis reveals an unconventional pathway of fatty acid synthesis in
990 cancer cells deficient for the mitochondrial citrate transport protein. *Metab Eng* 43: 198-207
991 Jiang L, Shestov AA, Swain P, Yang C, Parker SJ, Wang QA, Terada LS, Adams ND,
992 McCabe MT, Pietrak B, et al (2016) Reductive carboxylation supports redox homeostasis during
993 anchorage-independent growth. *Nature* 532: 255-258

994 Knights CD, Catania J, Di Giovanni S, Muratoglu S, Perez R, Swartzbeck A, Quong AA,
995 Zhang X, Beerman T, Pestell RG, et al (2006) Distinct p53 acetylation cassettes differentially
996 influence gene-expression patterns and cell fate. *J Cell Biol* 173(4):533-44 10.1083/jcb.200512059.
997 PMID: 16717128; PMCID: PMC2063863.

998 Kranendijk M, Struys EA, Salomons GS, Van der Knaap MS, Jakobs C (2012) Progress in
999 understanding 2-hydroxyglutaric acidurias. *J Inherit Metab Dis* 35: 571-587

1000 Kuleshov MV, Jones MR, Rouillard AD, Fernandez NF, Duan Q, Wang Z, Koplev S, Jenkins
1001 SL, Jagodnik KM, Lachmann A, et al (2016) Enrichr: a comprehensive gene set enrichment analysis
1002 web server 2016 update. *Nucleic Acids Res* 44: W90-7

1003 Liu B, Ghosh S, Yang X, Zheng H, Liu X, Wang Z, Jin G, Zheng B, Kennedy BK, Suh Y, et al
1004 (2012) Resveratrol rescues SIRT1-dependent adult stem cell decline and alleviates progeroid
1005 features in laminopathy-based progeria. *Cell Metab* 16: 738-750

1006 Losman JA, Kaelin WG (2013) What a difference a hydroxyl makes: mutant IDH, (R)-2-
1007 hydroxyglutarate, and cancer. *Genes Dev* 27: 836-852

1008 Maynard TM, Meechan DW, Dudevoir ML, Gopalakrishna D, Peters AZ, Heindel CC,
1009 Sugimoto TJ, Wu Y, Lieberman JA, Lamantia AS (2008) Mitochondrial localization and function of a
1010 subset of 22q11 deletion syndrome candidate genes. *Mol Cell Neurosci* 39: 439-451

1011 Mosaoa R, Kasprzyk-Pawelec A, Fernandez HR, Avantaggiati ML (2021) The Mitochondrial
1012 Citrate Carrier SLC25A1/CIC and the Fundamental Role of Citrate in Cancer, Inflammation and
1013 Beyond. *Biomolecules* 11: 141

1014 Murphey K, George PE, Pencheva B, Porter CC, Wechsler SB, Gambello MJ, Li H (2022)
1015 Acute myeloid leukemia and dilated cardiomyopathy in a pediatric patient with D-2-hydroxyglutaric
1016 aciduria type I. *Am J Med Genet A* 188: 2707-2711

1017 Nota B, Struys EA, Pop A, Jansen EE, Fernandez Ojeda MR, Kanhai WA, Kranendijk M, van
1018 Dooren SJ, Bevova MR, Sistermans EA, et al (2013) Deficiency in SLC25A1, encoding the
1019 mitochondrial citrate carrier, causes combined D-2- and L-2-hydroxyglutaric aciduria. *Am J Hum*
1020 *Genet* 92: 627-631

1021 Palmieri F, Scarcia P, Monné M (2020) Diseases Caused by Mutations in Mitochondrial
1022 Carrier Genes SLC25: A Review. *Biomolecules* 10: 655

1023 Patay Z, Mills JC, Löbel U, Lambert A, Sablauer A, Ellison DW (2012) Cerebral neoplasms in
1024 L-2 hydroxyglutaric aciduria: 3 new cases and meta-analysis of literature data. *AJNR Am J*
1025 *Neuroradiol* 33: 940-943

1026 Patay Z, Orr BA, Shulkin BL, Hwang SN, Ying Y, Broniscer A, Boop FA, Ellison DW
(2015) Successive distinct high-grade gliomas in L-2-hydroxyglutaric aciduria. *J Inherit Metab Dis* 38:
273-1028 277

1029 Phua YL, D'Annibale OM, Karunanidhi A, Mohsen AW, Kirmse B, Dobrowolski SF, Vockley J
1030 A multiomics approach reveals evidence for phenylbutyrate as a potential treatment for combined
1031 D,L-2- hydroxyglutaric aciduria. *Mol Genet Metab* [published online: May 15, 2024].
1032 10.1016/j.ymgme.2024.108495

1033 Poehlmann A, Habold C, Walluscheck D, Reissig K, Bajbouj K, Ullrich O, Hartig R, Gali-1034
Muhtasib H, Diestel A, Roessner A, et al (2011) Cutting edge: Chk1 directs senescence and mitotic
catastrophe in recovery from G_2 checkpoint arrest. *J Cell Mol Med* 15: 1528-1541.

Pop A, Williams M, Struys EA, Monné M, Jansen EEW, De Grassi A, Kanhai WA, Scarcia P,
1037 Ojeda MRF, Porcelli V, et al (2018) An overview of combined D-2- and L-2-hydroxyglutaric
aciduria: functional analysis of CIC variants. *J Inherit Metab Dis* 41: 169-180

1039 Prasun P, Young S, Salomons G, Werneke A, Jiang YH, Struys E, Paige M, Avantaggiati ML,
1040 McDonald M (2015) Expanding the Clinical Spectrum of Mitochondrial Citrate Carrier (SLC25A1)
1041 Deficiency: Facial Dysmorphism in Siblings with Epileptic Encephalopathy and Combined
D,L-2-1042 Hydroxyglutaric Aciduria. *JIMD Rep* 19: 111-115

1043 Rhinn M, Zapata-Bodalo I, Klein A, Plassat JL, Knauer-Meyer T, Keyes WM (2022) Aberrant
1044 induction of p19Arf-mediated cellular senescence contributes to neurodevelopmental defects. *PLoS*
1045 *Biol* 20: e3001664

1046 Rodríguez-García ME, Cotrina-Vinagre FJ, Cruz-Rojo J, Garzón-Lorenzo L, Carnicero-
1047 Rodríguez P, Pozo JS, Martínez-Azorín F (2018) A rare male patient with Fontaine progeroid
1048 syndrome caused by p.R217H de novo mutation in SLC25A24. *Am J Med Genet A* 176: 2479-2486

1049 Ruprecht JJ, Kunji ERS (2020) The SLC25 Mitochondrial Carrier Family: Structure and
1050 Mechanism. *Trends Biochem Sci* 45: 244-258

1051 Sasaki M, Knobbe CB, Itsumi M, Elia AJ, Harris IS, Chio II, Cairns RA, McCracken S,
1052 Wakeham A, Haight J, et al (2012) D-2-hydroxyglutarate produced by mutant IDH1 perturbs collagen
1053 maturation and basement membrane function. *Genes Dev* 26: 2038-2049

1054 Schmitt CA, Wang B, Demaria M (2022) Senescence and cancer - role and therapeutic
1055 opportunities. *Nat Rev Clin Oncol* 19: 619-636

1056 Smith A, McBride S, Marcadier JL, Michaud J, Al-Dirbashi OY, Schwartzentruber J, Beaulieu
1057 CL, Katz SL, Majewski J, Bulman DE, et al (2016) Severe Neonatal Presentation of Mitochondrial
1058 Citrate Carrier (SLC25A1) Deficiency. *JIMD Rep* 30: 73-79

1059 Srinivasan A, Zhou Y, Scordino T, Prabhu S, Wierenga A, Simon G, Wierenga KJ, Thompson
1060 J, Shah R, Sinha AA (2020) IDH1 mutated acute myeloid leukemia in a child with metaphyseal
1061 chondromatosis with D-2-hydroxyglutaric aciduria. *Pediatr Hematol Oncol* 37: 431-437

1062 Tan M, Mosaoa R, Graham GT, Kasprzyk-Pawelec A, Gadre S, Parasido E, Catalina-
1063 Rodriguez O, Foley P, Giaccone G, Cheema A, et al (2020) Inhibition of the mitochondrial citrate
1064 carrier, Slc25a1, reverts steatosis, glucose intolerance, and inflammation in preclinical models of
1065 NAFLD/NASH. *Cell Death Differ* 27: 2143-2157

1066 Stevens T, van der Werff Ten Bosch J, De Rademaeker M, Van Den Bogaert A, van den
1067 Akker M (2017) Risk of malignancy in 22q11.2 deletion syndrome. *Clin Case Rep* 5: 486-490

1068 Wang B, Varela-Eirin M, Brandenburg SM, Hernandez-Segura A, van Vliet T, Jongbloed EM,
1069 Wilting SM, Ohtani N, Jager A, Demaria M (2022) Pharmacological CDK4/6 inhibition reveals a p53-
1070 dependent senescent state with restricted toxicity. *EMBO J* 41: e108946

1071 Wiley CD, Campisi J (2021) The metabolic roots of senescence: mechanisms and
1072 opportunities for intervention. *Nat Metab* 3: 1290-1301

1073 Wiley CD, Velarde MC, Lecot P, Liu S, Sarnoski EA, Freund A, Shirakawa K, Lim HW, Davis
1074 SS, Ramanathan A, (2016) Mitochondrial Dysfunction Induces Senescence with a Distinct Secretory
1075 Phenotype. *Cell Metab* 23: 303-314

1076 Writzl K, Maver A, Kovačič L, Martinez-Valero P, Contreras L, Satrustegui J, Castori M, Faivre
1077 L, Lapunzina P, van Kuilenburg ABP, et al (2017) De Novo Mutations in SLC25A24 Cause a Disorder
1078 Characterized by Early Aging, Bone Dysplasia, Characteristic Face, and Early Demise. *Am J Hum*
1079 *Genet* 101: 844-855

1080 Xie N, Zhang L, Gao W, Huang C, Huber PE, Zhou X, Li C, Shen G, Zou B (2020) NAD+
1081 metabolism: pathophysiologic mechanisms and therapeutic potential. *Signal Transduct Target Ther* 5:
1082 227

1083 Xie Z, Bailey A, Kuleshov MV, Clarke DJB, Evangelista JE, Jenkins SL, Lachmann A,
1084 Wojciechowicz ML, Kropiwnicki E, Jagodnik KM, et al (2021) Gene Set Knowledge Discovery with
1085 Enrichr. *Curr Protoc* 1: e90

1086 Xu C, Shen WB, Reece EA, Hasuwa H, Harman C, Kaushal S, Yang P (2021) Maternal
1087 diabetes induces senescence and neural tube defects sensitive to the senomorphic rapamycin. *Sci*
1088 *Adv* 7: eabf5089

1089 Xu M, Tchkonia T, Ding H, Ogrodnik M, Lubbers ER, Pirtskhalava T, White TA, Johnson KO,
1090 Stout MB, Mezera V, et al (2015) JAK inhibition alleviates the cellular senescence-associated
1091 secretory phenotype and frailty in old age. *Proc Natl Acad Sci U S A* 112: E6301-10

1092 Zarei M, Hajihassani O, Hue JJ, Graor HJ, Loftus AW, Rathore M, Vaziri-Gohar A, Asara JM,
1093 Winter JM, Rothermel LD (2022) Wild-type IDH1 inhibition enhances chemotherapy response in
1094 melanoma. *J Exp Clin Cancer Res* 41: 283

1095 Zhao J, Yao K, Yu H, Zhang L, Xu Y, Chen L, Sun Z, Zhu Y, Zhang C, Qian Y, et al (2021)
1096 Metabolic remodelling during early mouse embryo development. *Nat Metab* 3: 1372-1384

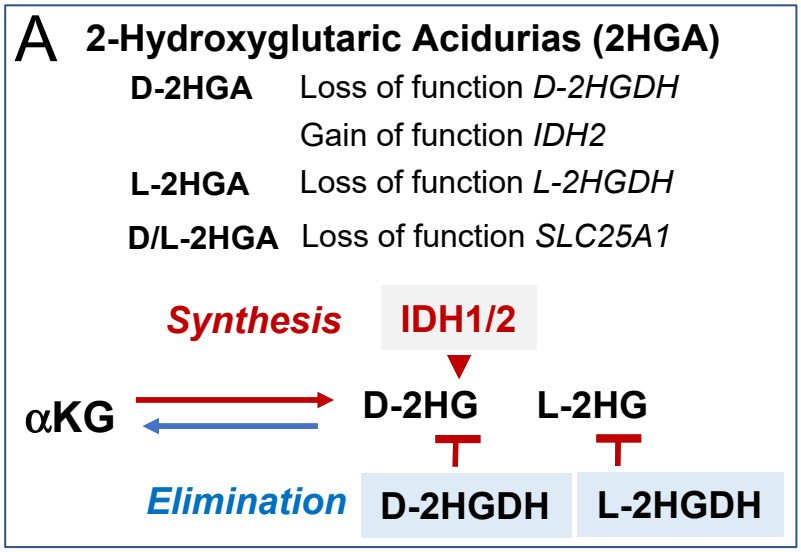
A
2-Hydroxyglutaric Acidurias (2HGA)
D-2HGA
Loss of function D-2HGDH
Gain of function IDH2
L-2HGA
Loss of function L-2HGDH
D/L-2HGA
Loss of function SLC25A1
Synthesis
IDH1/2
αKG
D-2HG
L-2HG
Elimination
D-2HGDH
L-2HGDH

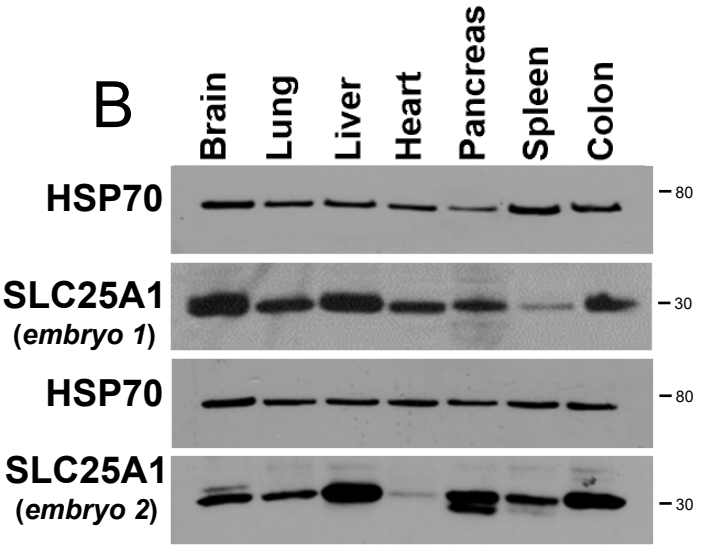
B
Brain
Lung
Liver
Heart
Pancreas
Spleen
Colon
HSP70
80
SLC25A1
(embryo 1)
30
HSP70
80
SLC25A1
(embryo 2)
30

C
5 mm

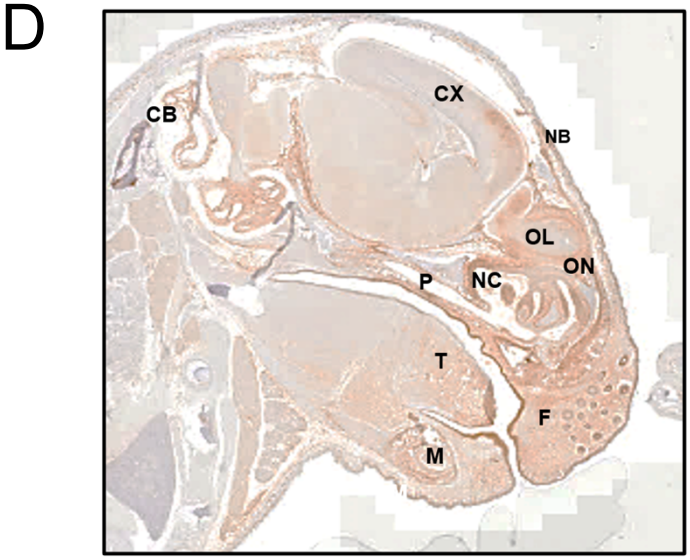
D
CB
CX
NB
OL
ON
P
NC
T
F
M

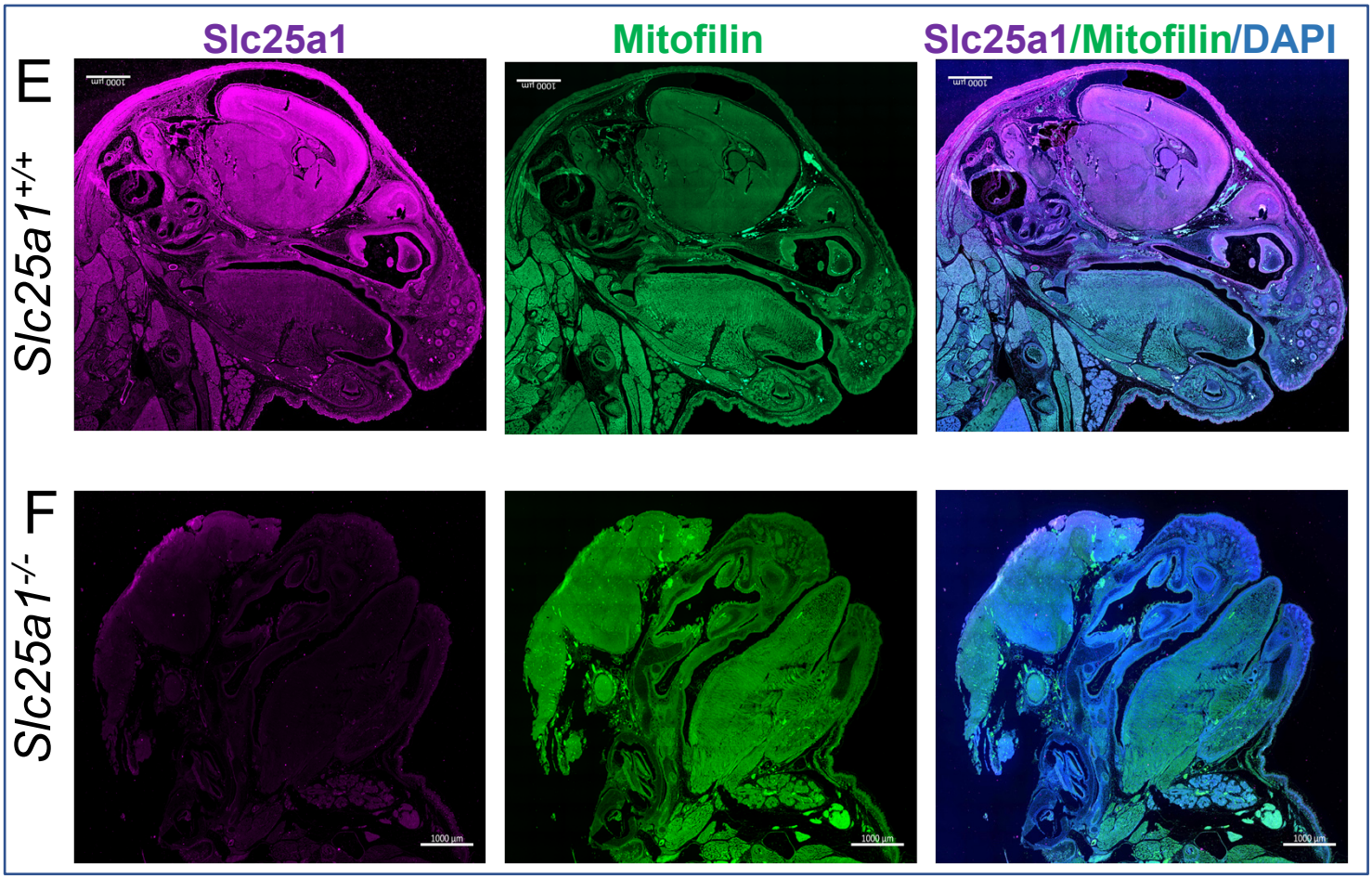
Slc25a1
Mitofilin
Slc25a1/Mitofilin/DAPI
E
Slc25a1+/+
F
Slc25a1-/-
1000 µm

Figure 1. Analysis of SLC25A1 protein expression.

(**A**) Schematic representation of 2-Hydroxyglutaric acidurias (2HGA). Upper panel: genetic alterations in individual and combined 2-HGAs. Lower panel: main pathways to the synthesis and elimination of D- and L-2HG. (**B**) Expression levels of SLC25A1 protein in the indicated organs derived from two *Slc25a1* wild-type embryos at E19.5 dpf. (**C-D**) Representative IHC images with the anti-SLC25A1 antibody staining in embryos at E19 dpf. Cb= Cerebellum, Cx= Cerebral cortex, F=follicle, P=palate, T=tongue, M=mandible, NB= nasal bone, NC= nasal cavity, OL=olfactory lobe, ON=olfactory nerve. (**E**) Staining with anti-SLC25A1, anti-mitofilin and DAPI in embryos at E19 dpf. Bar=1000 μm. **(F)** Staining as in E in E19 dpf *SLC25A1* nullizygous embryos.

A

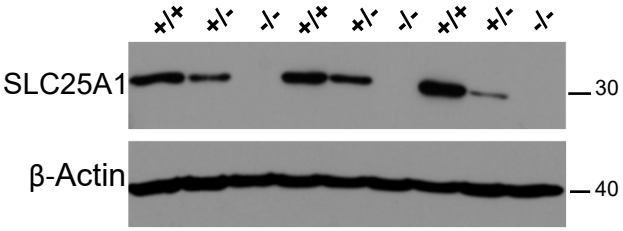

B

Embryos		
GT	Total	%
+/+	136	27
+/-	258	53
-/-	101	20
Tot.	495	

C

Births		
GT	Total #.	%
+/+	48	30.38
+/-	99	62.66
-/-	11	6.96
Total	158	

D

Phenotype	Total #	%
Exencephaly	36	43.90
Cleft palate/ flat face	40	48.78
Small size	62	75.61
Pale/anemic	23	28.05

E

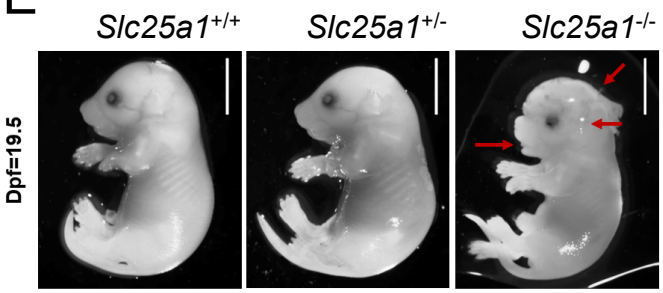

F

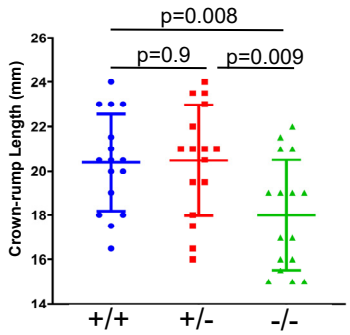

G

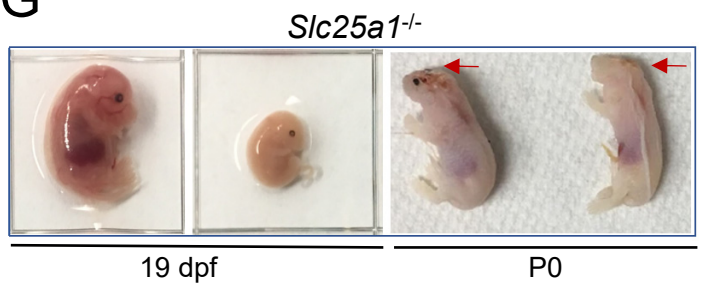

H

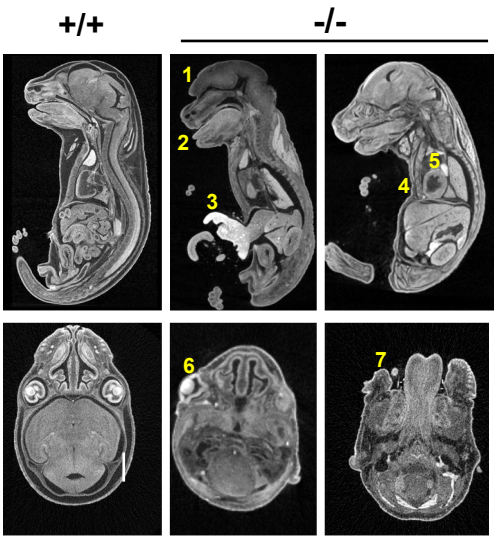

I

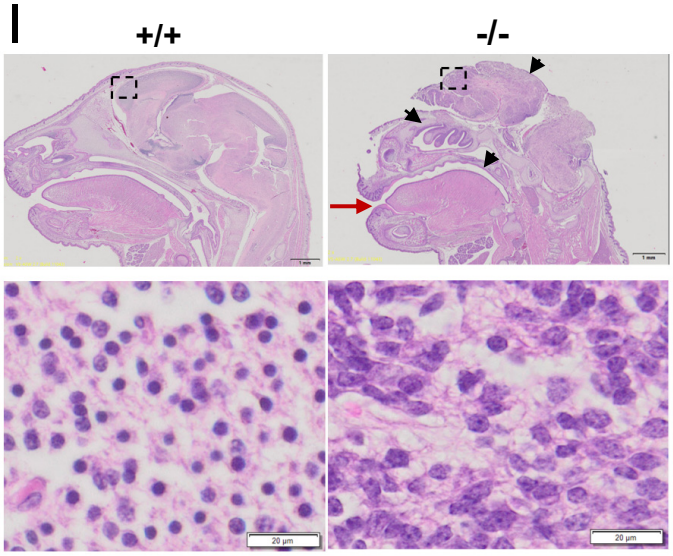

J

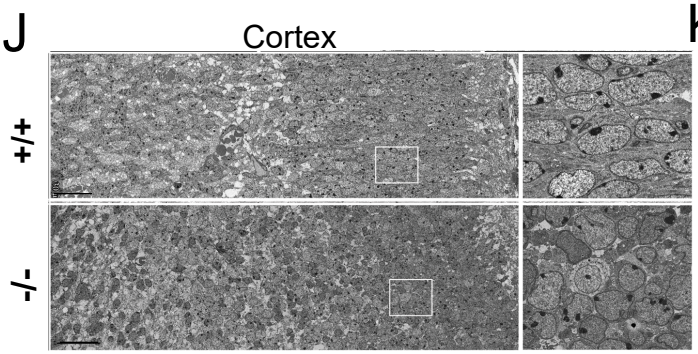

K

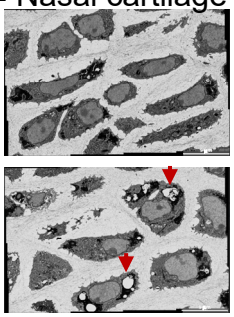

L

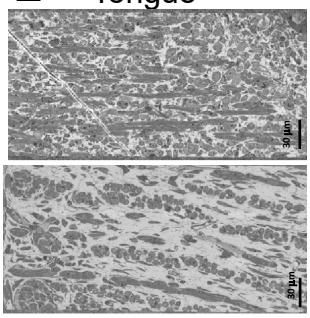

Figure 2. The knock-out of the *Slc25a1* gene leads to perinatal lethality and to multiple abnormalities.

(**A)** Representative immunoblot showing the SLC25A1 protein expression in MEFs cells isolated from *Slc25a1*$^{+/+}$, *Slc25a1*$^{+/-}$ and *Slc25a1*$^{-/-}$ embryos (n=3 per genotype). The antibody used in this blot is a polyclonal antibody raised against full length human SLC25A1, but other antibodies yielded similar results. (**B**) Representation of the genotypes observed across 85 litters (495 mice) obtained by breeding *Slc25a1* heterozygous mice.

(**C**) Number and percentage of births observed across a population of newborn *Slc25a1*$^{-/-}$ mice.

(**D**) Prevalence of the phenotypic alterations observed in *Slc25a1*$^{-/-}$ embryos.

(**E**) Representative images of *Slc25a1*$^{+/+}$, *Slc25a1*$^{+/-}$ and *Slc25a1*$^{-/-}$ embryos under stereoscopic microscope at E18.5 dpf. Red arrows point to cleft palate, underdeveloped ears and brain abnormalities. Bar=5 mm.

(**F**) Measurements of crows to rump length showing smaller body size in *Slc25a1* homozygous mice compared with wild-type and heterozygous littermates (n= 16 mice per genotype, respectively). p-values were calculated with two tailed non parametric t-test.

(**G**) Heterogeneity of the phenotypes of *Slc25a1*$^{-/-}$ embryos at 19pdf or at P0, showing variations in body size, lack of skull and eyes in the last two embryos on left (indicated by arrows).

(**H**) Computed Tomography (CT) scan of wild-type or *Slc25a1*$^{-/-}$ embryos at E18.5 dpf. Yellow numbers indicate: 1: Excencephaly; 2: Protruding tongue; 3: Gastroschisis; 4: Pectus excavatum; 5: Abnormal heart. 6: Abnormal eye; 7: Abnormal facial area morphology. Bar=1mm.

(**I**) Representative images of H&E staining in the embryos of the indicated genotype. Top panels show the anatomy of the whole head; lower panels show magnification of the cortical region and nuclear abnormalities in *Slc25a1*$^{-/-}$ mice. Bar= 20 μm. Red arrow points to hypertrophic tongue.

(**J-L**) Scanning electron microscopy (SEM) overviews of the neocortex (**J**), nasal cartilage (**K**) and tongue (**L**) in wild-type and *Slc25a1*$^{-/-}$ embryos at E18.5 dpf. Arrows in K point to vacuolization in the nasal cartilage.

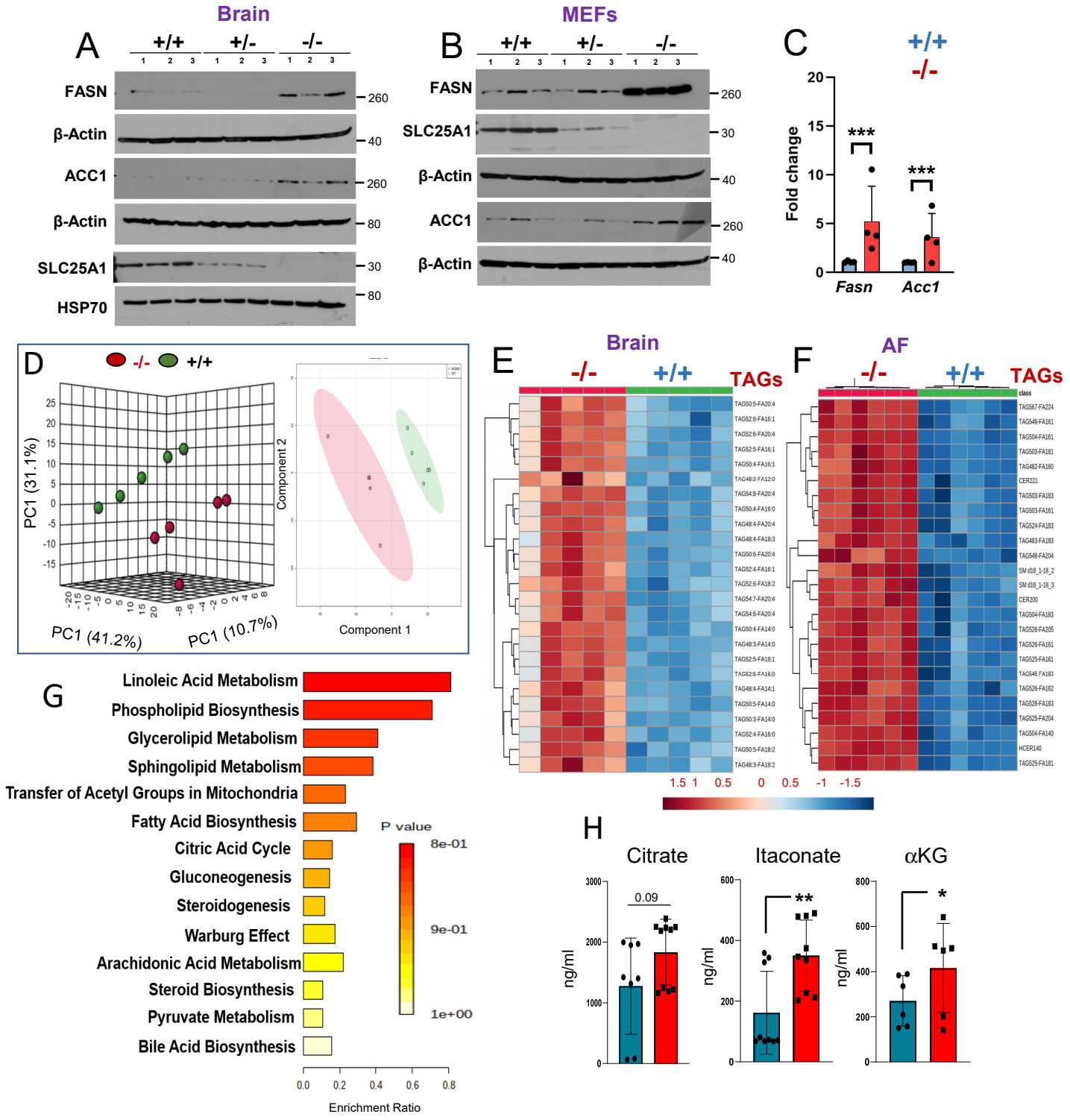
A
Brain
+/+
+/-
-/-
FASN
β-Actin
ACC1
β-Actin
SLC25A1
HSP70
260
40
260
80
30
80
B
MEFs
+/+
+/-
-/-
FASN
SLC25A1
β-Actin
ACC1
β-Actin
260
30
40
260
40
C
+/+
-/-
Fold change
***
***
Fasn
Acc1
D
-/-
+/+
PC1 (31.1%)
PC1 (41.2%)
PC1 (10.7%)
Component 2
Component 1
E
Brain
-/-
+/+
TAGs
F
AF
-/-
+/+
TAGs
G
Linoleic Acid Metabolism
Phospholipid Biosynthesis
Glycerolipid Metabolism
Sphingolipid Metabolism
Transfer of Acetyl Groups in Mitochondria
Fatty Acid Biosynthesis
Citric Acid Cycle
Gluconeogenesis
Steroidogenesis
Warburg Effect
Arachidonic Acid Metabolism
Steroid Biosynthesis
Pyruvate Metabolism
Bile Acid Biosynthesis
P value
8e-01
9e-01
1e+00
Enrichment Ratio
H
Citrate
Itaconate
αKG
ng/ml
0.09
**
*

Figure 3. Loss of *Slc25a1 l*eads to metabolic remodeling.

(A-B) Expression of the indicated proteins in brain (**A**) and MEFs (**B**) isolated from *Slc25a1*$^{+/+}$, *Slc25a1*$^{+/-}$ and *Slc25a1*$^{-/-}$ embryos (n=3 per genotype).

(**C**) mRNA levels detected with q-RT-PCR of the indicated genes in MEFs *Slc25a1*$^{+/+}$ (blue) and *Slc25a1*$^{-/-}$ (red). Each dot represents MEFs isolated from a different mouse.

(**D**) Principal component analysis (PCA) scores plot and the partial least squares (PLS) of 5 wild-type and *Slc25a1* nullyzygous embryos used for metabolic studies.

(**E-F**) Heatmap of top 25 enriched lipids in brain and AF samples obtained from *Slc25a1*$^{+/+}$ (green) and *Slc25a1*$^{-/-}$ (red) (n=5, from different litters, each in triplicate). Normalization was performed by dividing area under the curve for each metabolite by internal standard area. Clustering was performed by using the Metaboanalyst software.

(**G**) Pathway enrichment analysis in amniotic fluid obtained from *Slc25a1*$^{-/-}$ embryos relative to wild-type (n=3 per genotype, each in 3 technical replicates).

(**H**) Concentrations of the indicated TCA intermediates in the amniotic fluid obtained from *Slc25a1*$^{+/+}$ and *Slc25a1*$^{-/-}$ embryos (n=3-5, each in technical replicates). All data are presented as mean value ± SD. Unpaired non parametric t-test was used throughout.

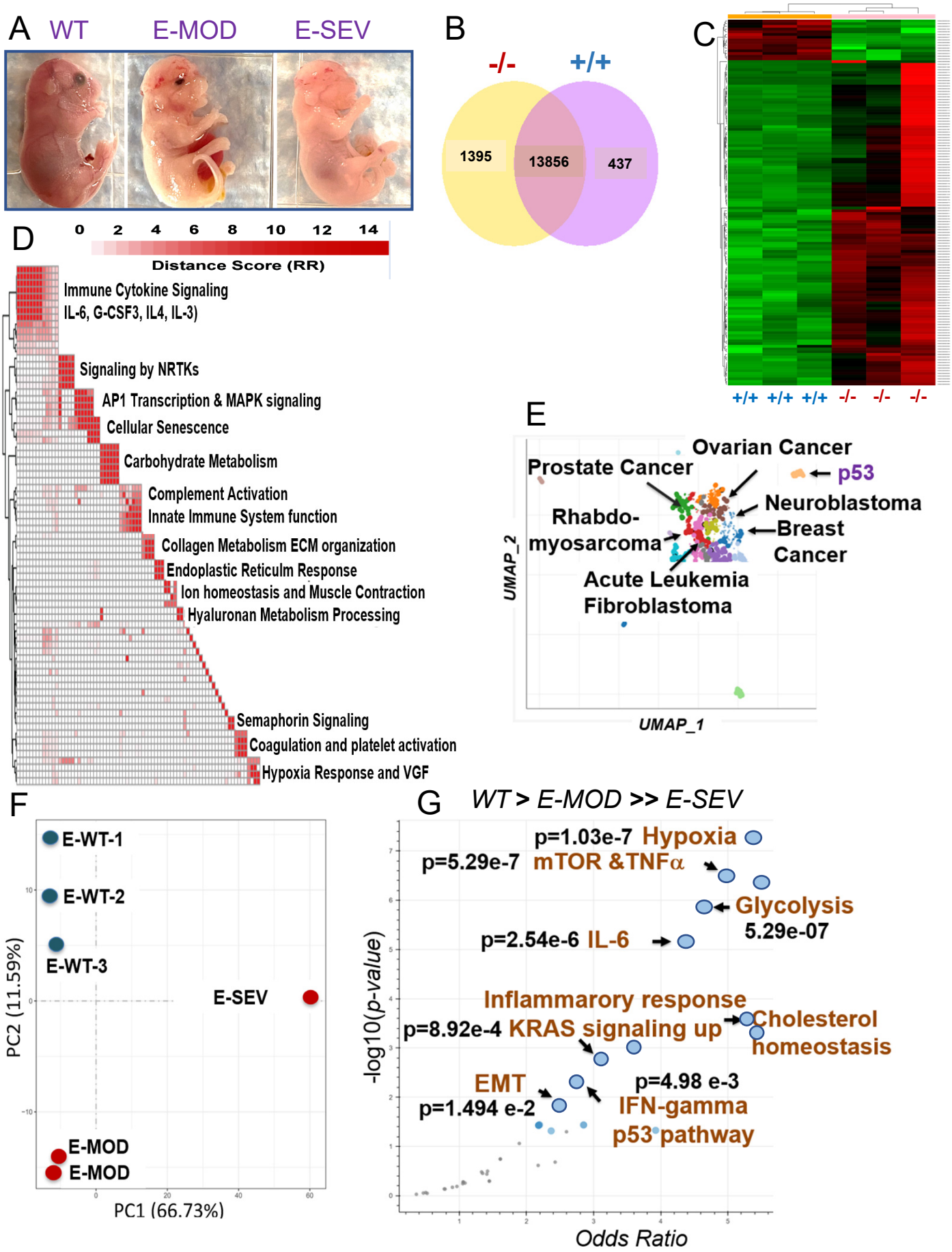
A
WT
E-MOD
E-SEV
B
-/-
+/+
1395
13856
437
C
+/+ +/+ +/+ -/- -/- -/-
D
0 2 4 6 8 10 12 14
Distance Score (RR)
Immune Cytokine Signaling
IL-6, G-CSF3, IL4, IL-3)
Signaling by NRTKs
AP1 Transcription & MAPK signaling
Cellular Senescence
Carbohydrate Metabolism
Complement Activation
Innate Immune System function
Collagen Metabolism ECM organization
Endoplastic Reticulm Response
Ion homeostasis and Muscle Contraction
Hyaluronan Metabolism Processing
Semaphorin Signaling
Coagulation and platelet activation
Hypoxia Response and VGF
E
Ovarian Cancer
Prostate Cancer
p53
Neuroblastoma
Rhabdo-
myosarcoma
Breast
Cancer
Acute Leukemia
Fibroblastoma
UMAP_2
UMAP_1
F
E-WT-1
E-WT-2
E-WT-3
E-SEV
E-MOD
E-MOD
PC2 (11.59%)
PC1 (66.73%)
G
WT > E-MOD >> E-SEV
p=1.03e-7 Hypoxia
p=5.29e-7 mTOR &TNFα
Glycolysis
5.29e-07
p=2.54e-6 IL-6
Inflammarory response
p=8.92e-4 KRAS signaling up
Cholesterol
homeostasis
EMT
p=4.98 e-3
p=1.494 e-2
IFN-gamma
p53 pathway
-log10(p-value)
Odds Ratio

Figure 4. Transcriptional analysis of *Slc25a1* deficient embryos.

(**A**) Representative phenotypes of *Slc25a1*$^{-/-}$ mice classified based on the severity of the phenotype (E18-19 dpf).

(**B**) Venn diagram representing genes differentially regulated in the brains isolated from *Slc25a1*$^{+/+}$ and *Slc25a1*$^{-/-}$ embryos at 18.5 dpc (n=3).

(**C**) Hierarchical clustering map of differentially expressed genes as in B.

(**D**) Pathway enrichment analysis of genes significantly elevated in *Slc25a1*$^{-/-}$ mice relative to wild-type. All significantly enriched pathways (FDR<0.05), assessed from the Reactome Database, were clustered *via* a distance metric derived from shared significant genes common amongst enriched gene sets. Clustered gene sets were summarized by biological function.

(**E**) Scatter plot of enriched transcriptomic signature (with ChEA). (p=<0.05).

(**F**) PCA plot of the transcriptomic profiles of indicated embryos.

(**G**) Transcriptomic data derived from each of the embryos were used for a Hue-Saturation-Value (HSV) analysis. The Enrichr gene set tool was employed to identify gene sets that are significantly more active in E-SEV and moderately elevated in E-MOD *versus* wild-type (*WT* **>** *E-MD* **>>** *E-SV);* p< 0.05.

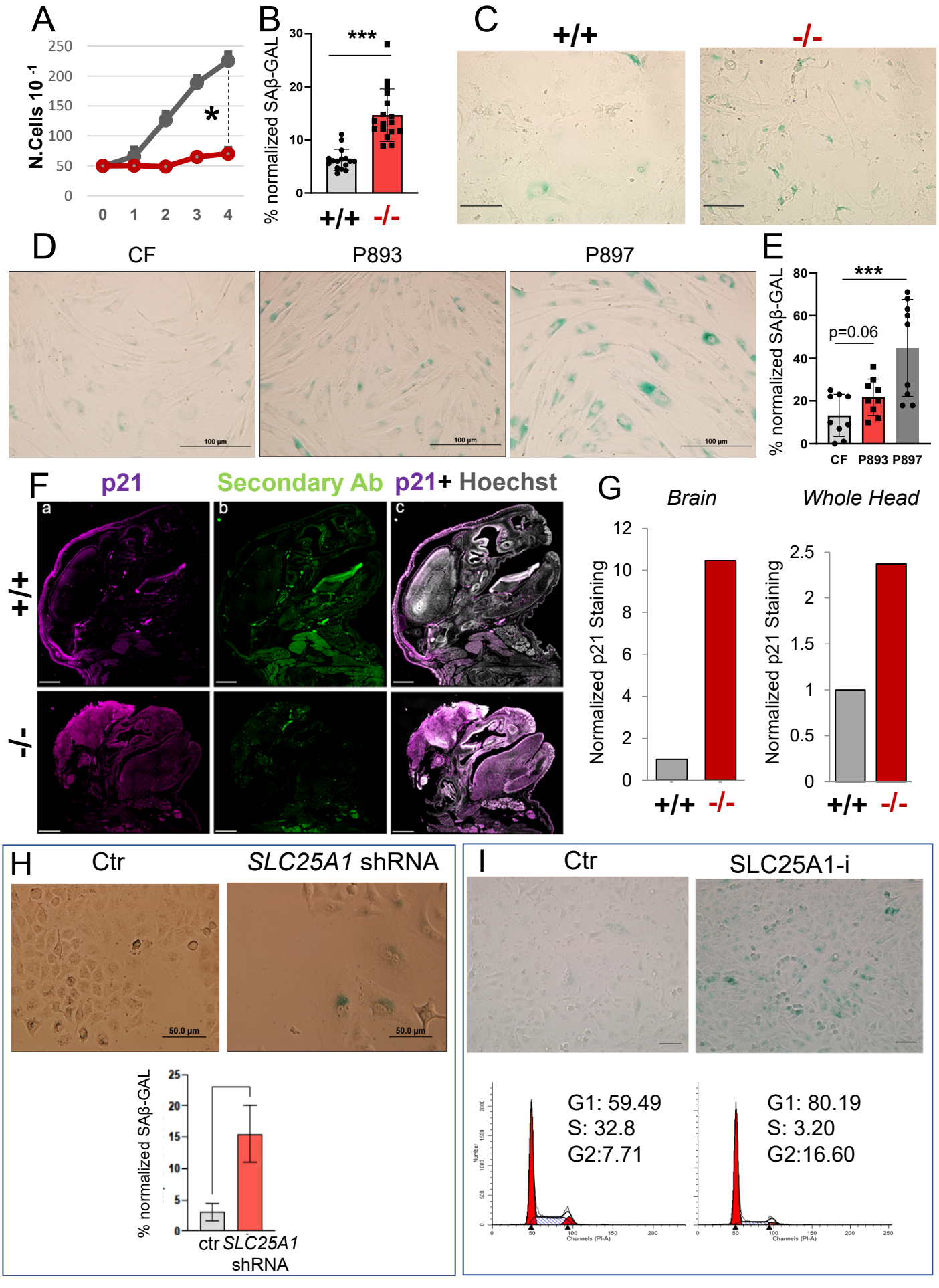
A
N.Cells 10 -1
250
200
150
100
50
0
0 1 2 3 4
*
B
% normalized SAβ-GAL
30
20
10
0
***
+/+ -/-
C
+/+
-/-
D
CF
P893
P897
100 µm
E
% normalized SAβ-GAL
80
60
40
20
0
***
p=0.06
CF P893 P897
F
p21
Secondary Ab
p21+ Hoechst
a
b
c
+/+
-/-
G
Brain
Whole Head
Normalized p21 Staining
12
10
8
6
4
2
0
2.5
2
1.5
1
0.5
+/+ -/-
H
Ctr
SLC25A1 shRNA
50.0 µm
% normalized SAβ-GAL
25
20
15
10
5
0
ctr SLC25A1 shRNA
I
Ctr
SLC25A1-i
G1: 59.49
S: 32.8
G2:7.71
G1: 80.19
S: 3.20
G2:16.60
Channels (PI-A)

Figure 5. Induction of premature senescence in cells and tissues lacking SLC25A1.

(**A**) Growth curves of MEF cells isolated from *Slc25a1*$^{+/+}$ and *Slc25a1*$^{-/-}$ embryos.

(**B-C**) Quantification of the SA-β-GAL positive MEF cells (%) normalized to the total number of cells identified with DAPI counter-staining pooled from two independent experiments and representative images of (SA-β-GAL) activity.

(**D-E)** Representative images of SA-β-GAL staining in human fibroblasts (**D**) and quantification of the SA-β-GAL positive cells normalized to the total number of cells identified with DAPI counter-staining.

(**E**). All IF data are presented as a % positive cells ± SD pooled from two independent experiments. Bar=100 μm.

(**F**) p21 immunofluorescence staining of the head of *Slc25a1*$^{+/+}$ and *Slc25a1*$^{-/-}$ embryos (E19 dpf). Hoechst was used to counterstain the nuclei. Secondary antibody alone was used as a control. Bar= 1000 μM.

(**G**) Quantification of experiments shown in F with imageJ representing particle counts normalized to DAPI of the brain or whole head.

(**H**) A549 cells were transduced with the control lentivirus or with lentivirus harboring the SLC25A1 specific shRNA (see Fig.10 for SLC25A1 levels), selected with puromycin for 5 days and stained with β-GAL.

(**I**) SA-β-GAL activity and cell cycle analysis of A549 cells treated with the SLC25A1-i.

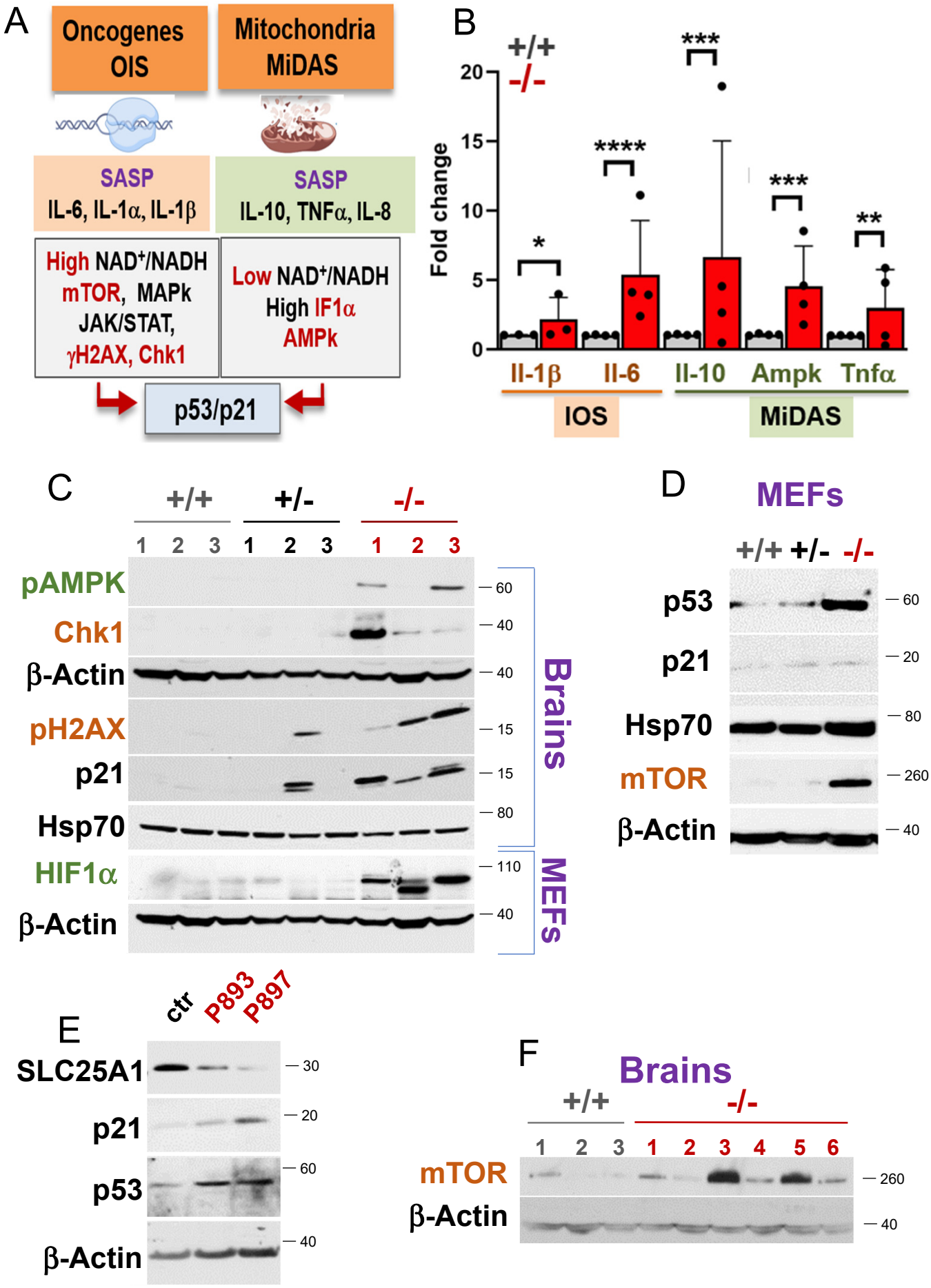
A
Oncogenes
OIS
Mitochondria
MiDAS
SASP
IL-6, IL-1α, IL-1β
SASP
IL-10, TNFα, IL-8
High NAD+/NADH
mTOR, MAPk
JAK/STAT,
γH2AX, Chk1
Low NAD+/NADH
High IF1α
AMPk
p53/p21
B
+/+
-/-
Fold change
20
15
10
5
0
*
****
***
***
**
Il-1β
Il-6
Il-10
Ampk
Tnfα
IOS
MiDAS
C
+/+
+/-
-/-
1 2 3 1 2 3 1 2 3
pAMPK
Chk1
β-Actin
pH2AX
p21
Hsp70
HIF1α
β-Actin
60
40
40
15
15
80
110
40
Brains
MEFs
D
MEFs
+/+ +/- -/-
p53
p21
Hsp70
mTOR
β-Actin
60
20
80
260
40
E
ctr
P893
P897
SLC25A1
p21
p53
β-Actin
30
20
60
40
F
Brains
+/+
-/-
1 2 3 1 2 3 4 5 6
mTOR
β-Actin
260
40

Figure 6. SLC25A1 dysfunction induces the OIS and MIDAS pathways of senescence.

(**A**) Scheme of the OIS and MiDAS pathways of senescence and of the associated SASPs, depicting DNA replication stress or mitochondrial dysfunction, respectively (see also text for explanation) (*created with Biorender*).

(**B**) mRNA levels of the IOS (brown) and MiDAS (green) SASPs in MEFs *Slc25a1*$^{+/+}$ (grey) and *Slc25a1*$^{-/-}$ (red) respectively (n=3-4).

(**C-F**) Expression level of the indicated proteins involved in IOS (brown) and MiDAS (green) in the brain samples (**C,F**), MEFs (**C**,**D**) and in the patient's fibroblasts (**E**) (n=1-6).

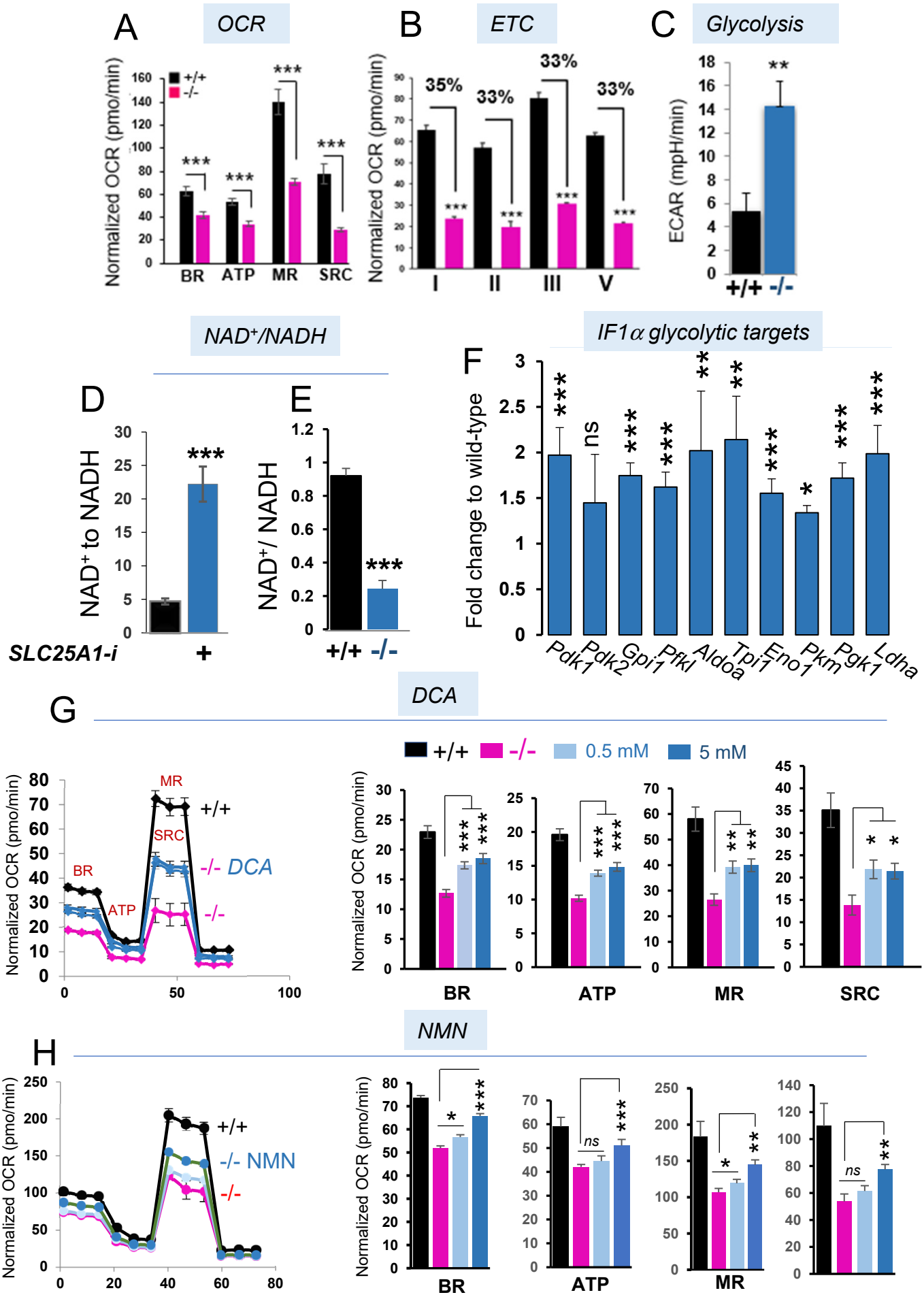
A
OCR
Normalized OCR (pmo/min)
+/+
-/-
BR
ATP
MR
SRC
B
ETC
35%
33%
33%
33%
I
II
III
V
C
Glycolysis
ECAR (mpH/min)
+/+
-/-
NAD+/NADH
D
NAD+ to NADH
SLC25A1-i
+
E
NAD+/ NADH
+/+
-/-
IF1α glycolytic targets
F
Fold change to wild-type
Pdk1
Pdk2
Gpi1
Pfkl
Aldoa
Tpi1
Eno1
Pkm
Pgk1
Ldha
ns
G
DCA
+/+
-/-
0.5 mM
5 mM
MR
SRC
BR
ATP
-/- DCA
-/-
H
NMN
+/+
-/- NMN
-/-
ns

Figure 7. Cells lacking SLC25A1 undergo mitochondrial respiration deficit.

(**A**) Oxygen consumption rate (OCR) was assessed using Seahorse Extracellular Flux Analyzer in MEFs isolated from *Slc25a1*$^{+/+}$ (black) and *Slc25a1*$^{-/-}$ (pink) embryos. Injection of Oligomycin, FCCP and Rotenone/Antimycin allowed calculation of the BR= Basal respiration; ATP= ATP Production, MR= Maximal Respiration, SRC= Spare Respiratory Capacity.

(**B**) Activities of the indicated ETC complexes measured in the $^{+/+}$ or $^{-/-}$ MEFs. % = residual activity.

(**C**) Glycolysis in the indicated group of MEFs measured as Extracellular acidification (ECAR).

(**D**) Enzymatic activity assay using LDH-A in cell extracts derived from cells untreated or treated with the SLC25A1-i, and measured by absorbance at 340nm, as rate of conversion of NAD^+ to NADH.

(**E**) NAD^+/NADH ratio in freshly isolated MEFs from *Slc25a1*$^{+/+}$ and *Slc25a1*$^{-/-}$ embryos.

(**F**) Relative expression of indicated HIF1α genes/transcripts in brains isolated from *Slc25a1*$^{+/+}$ and *Slc25a1*$^{-/-}$ embryos.

(**G-H**) OCR measured in *Slc25a1*$^{+/+}$ and $^{-/-}$ MEFs untreated or treated with the indicated concentration of DCA (**G**) for 4 hrs, or NMN (**H**) for 16 hrs at 50 and 100 uM. Bars represent SD and p-values were calculated using two tailed non parametric t-test.

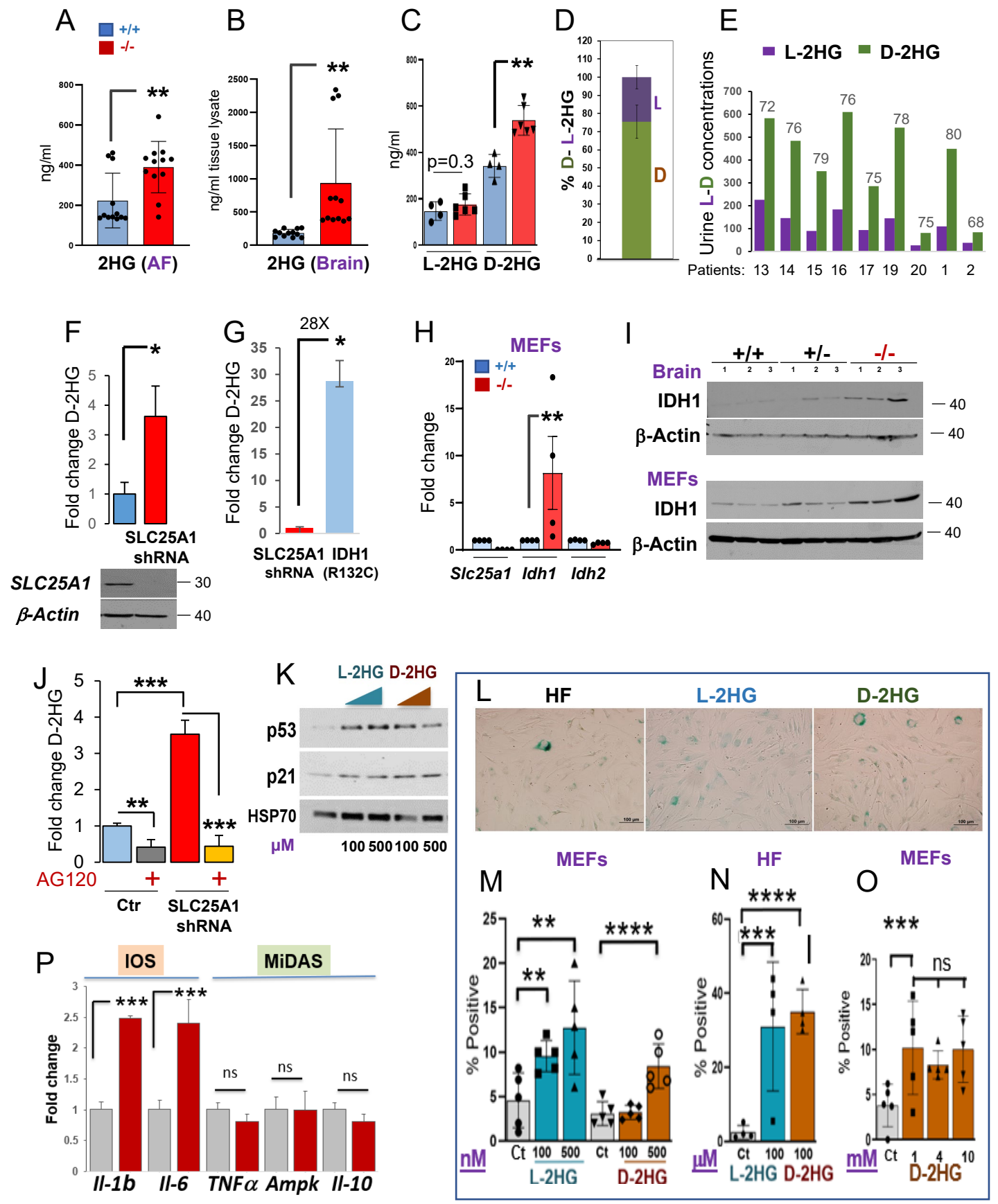
A
+/+
-/-
ng/ml
2HG (AF)
B
ng/ml tissue lysate
2HG (Brain)
C
ng/ml
p=0.3
L-2HG D-2HG
D
% D- L-2HG
L
D
E
L-2HG D-2HG
Urine L-D concentrations
Patients: 13 14 15 16 17 19 20 1 2
F
Fold change D-2HG
SLC25A1 shRNA
SLC25A1
β-Actin
G
28X
Fold change D-2HG
SLC25A1 shRNA
IDH1 (R132C)
H
MEFs
Fold change
Slc25a1 Idh1 Idh2
I
+/+ +/- -/-
Brain
IDH1
β-Actin
MEFs
IDH1
β-Actin
J
Fold change D-2HG
AG120
Ctr
SLC25A1 shRNA
K
L-2HG D-2HG
p53
p21
HSP70
μM 100 500 100 500
L
HF
L-2HG
D-2HG
M
MEFs
% Positive
nM
Ct 100 500 Ct 100 500
L-2HG D-2HG
N
HF
% Positive
μM
Ct 100 100
L-2HG D-2HG
O
MEFs
% Positive
mM
Ct 1 4 10
D-2HG
P
IOS
MiDAS
Fold change
Il-1b Il-6 TNFα Ampk Il-10

Figure 8. 2HG induces the IOS pathway of senescence.

(**A-B**) 2HG enrichment in the amniotic fluid (**A**) and brain samples (**B**) obtained from *Slc25a1*$^{+/+}$ (blue) and *Slc25a1*$^{-/-}$ (red) embryos at E18.5 dpf (n=4).

(**C**) D-L- 2HG enrichment in the amniotic fluids of *Slc25a1*$^{+/+}$ (blue) and *Slc25a1*$^{-/-}$ (red) embryos (n=4-5).

(**D**) Relative abundance of D- and L- 2HG (%) in the amniotic fluid samples of *Slc25a1*$^{-/-}$ embryos compared to wild-type littermates (n=2-3).

(**E**) Urine D- and L- 2HG concentration in patient samples. Data were extrapolated based on enrichment detected in two different studies. Patients 13-20 were from ref. 8; Patients 1 and 2 from ref. 11.

(**F**) D-2HG enrichment in A549 cells harboring the shRNA mediated *SLC25A1* knock-down relative to control.

(**G**) D-2HG enrichment in cells harboring the SLC25A1-KD or expressing IDH1$^{\mathbf{R132C}}$.

(**H-I**) mRNA (**H**) and protein (**I**) levels of SLC25A1, IDH1 and IDH2 in the indicated MEFs or brain samples.

(**J**) D-2HG enrichment in A549 cells harboring the SLC25A1-shRNA treated with AG120. Results were obtained from 3 experiments combined.

(**K**) Expression levels of p53 and p21 in human fibroblast treated with the indicated concentrations of L- or D-2HG.

(**L**) Representative images of SA-β-GAL staining of control human fibroblast cells treated with indicated L-or D-2HG for 72 hours (Bar= 100 μM).

(**M-O**) Quantification of SA-β-GAL staining of MEFs cells (**M,O**) or control human fibroblasts (HF, **N**) treated with indicated concentrations of L-or D-2HG for 3 to 5 days (Bar= 100 μM). Bars are SD from 2 experiments.

(**P**) mRNA levels of the IOS (brown) and MiDAS (green) SASPs in cells treated with D-2HG. Data are presented as mean value ± SD and p-values were calculated using unpaired t-test.

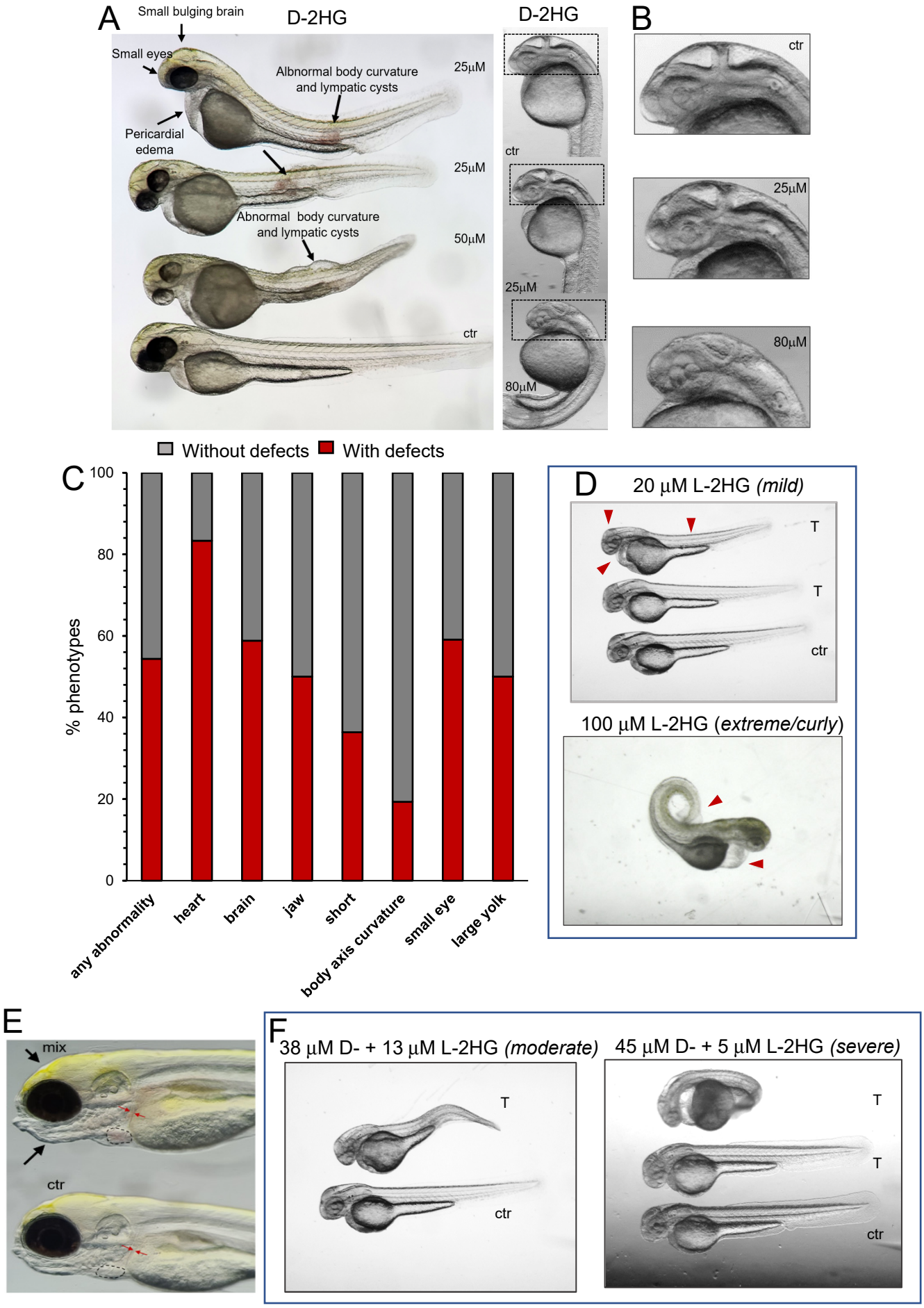
A
Small bulging brain
D-2HG
Small eyes
Albnormal body curvature
and lympatic cysts
25μM
Pericardial
edema
25μM
Abnormal body curvature
and lympatic cysts
50μM
ctr
D-2HG
ctr
25μM
80μM
B
ctr
25μM
80μM
Without defects
With defects
C
% phenotypes
100
80
60
40
20
0
any abnormality
heart
brain
jaw
short
body axis curvature
small eye
large yolk
D
20 μM L-2HG (mild)
T
T
ctr
100 μM L-2HG (extreme/curly)
E
mix
ctr
F
38 μM D- + 13 μM L-2HG (moderate)
T
ctr
45 μM D- + 5 μM L-2HG (severe)
T
T
ctr

Figure 9. 2HG perturbs embryonic development in zebrafish embryos.

(**A**) Phenotypes of 25 μM or 50 μM D-2HG treated embryos at 2 dpf. Embryos were injected at blastula-stage. Prominent alterations are small eyes, bulging brains, enlarged yolk sack, pericardial edema, altered body curvature, reduced body length, lymphatic cysts, and disorganized cellular structure of tissues, most prominently seen in the brain.

(**B**) Phenotypes of 25 μM or 80 μM D-2HG treated embryos at 36 hpf. Top embryo is control. Higher magnification images of the head show the dose-dependent tissue disorganization of the brain.

(**C**) Percent of zebrafish with or without defects untreated or treated with 2HG (control n=4-15, 2HG treated n=18-57). Data represent the results of at least 3 repetition experiments of embryos treated with different doses of 2HG.

(**D**) Phenotype of embryos treated with the indicated doses of Octyl-S-2HG at the indicated concentrations. Red arrows point to alterations in brain size, pericardial edema, enhanced body curvature and enlarged yolk.

(**E**) Five days dpf Casper larvae. The top fish was treated with 30 μM D-2HG plus 20 μM L-2HG at 1 dpf. The lower fish is control. The treated larva has an enlarged heart (outlined with dashed line) and large diameter blood vessels (indicated with arrows). The treated larva additionally has a dysmorphic jaw and slightly bulging brain.

(**F**) Treatment of embryos at 36 hpf, with the indicated mixtures using different ratios of D-2HG and L-2HG.

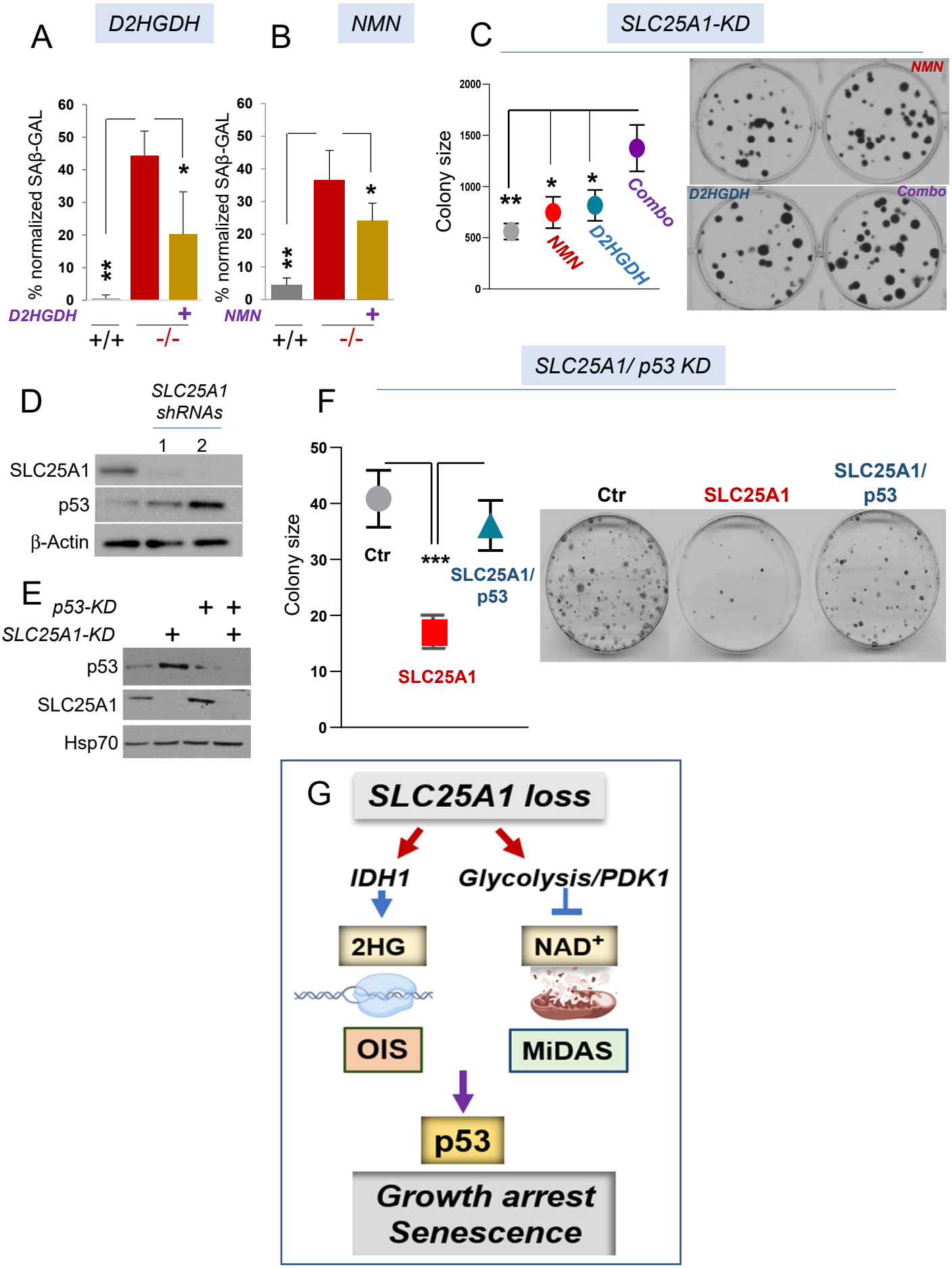
A
D2HGDH
% normalized SAβ-GAL
60
50
40
30
20
10
0
**
*
D2HGDH
+
+/+
-/-
B
NMN
% normalized SAβ-GAL
60
50
40
30
20
10
0
**
*
NMN
+
+/+
-/-
C
SLC25A1-KD
Colony size
2000
1500
1000
500
0
**
*
*
NMN
D2HGDH
Combo
NMN
D2HGDH
Combo
D
SLC25A1
shRNAs
1
2
SLC25A1
p53
β-Actin
E
p53-KD
+
+
SLC25A1-KD
+
+
p53
SLC25A1
Hsp70
F
SLC25A1/ p53 KD
Colony size
50
40
30
20
10
0
Ctr
***
SLC25A1/
p53
SLC25A1
Ctr
SLC25A1
SLC25A1/
p53
G
SLC25A1 loss
IDH1
Glycolysis/PDK1
2HG
NAD+
OIS
MiDAS
p53
Growth arrest
Senescence

Figure 10. The growth defect imposed by *SLC25A1* deficiency is p53-dependent.

(A-B) Quantification of the SAβ-GAL positive (%) MEF cells in the presence or absence of D2HGDH (**A**) or treated with NMN (**B**) and normalized to the total number of cells identified with DAPI counter-staining.

(**C**) Quantification (with ImageJ) and representative images of colony formation assay of cells transduced with the lentivirus harboring the SLC25A1-shRNA (SLC25A1-KD) and treated with NMN, or over-expressing D2HGDH, alone or in combination (indicated as *combo*).

(**D**) SLC25A1 and p53 expression levels in A549 cells transduced with the control lentivirus (pLKO, ctr) or with lentivirus vectors harboring two different SLC25A1 shRNAs (1 and 2).

(**E**) Levels of expression of SLC25A1 and p53 in the double knock-down experiments performed in A549 cells.

(**F**) Colony formation assay in A549 cells in the presence and absence of the Slc25a1-KD and of the p53-KD alone, or in combination. Quantification of colonies size was performed with ImageJ using multiple plates and bars represent SD. Unpaired non parametric t test was used.

(**G**) Model representing the effects of *SLC25A1* loss (see also the discussion), and depicting the main pathways identified in this study leading to the induction of the IOS and MiDAS programs.